The Astronomical Journal, 140:1347–1369, 2010 November doi:10.1088/0004-6256/140/5/1347

THE DUSTY NOVA V1065 CENTAURI (NOVA CEN 2007): A SPECTROSCOPIC ANALYSIS OF ABUNDANCES AND DUST PROPERTIES

L. Andrew Helton[1], Charles E. Woodward[1], Frederick M. Walter[2], Karen Vanlandingham[3], Greg J. Schwarz[4], Aneurin Evans[5], Jan-Uwe Ness[6], Thomas R. Geballe[7], Robert D. Gehrz[1], Matthew Greenhouse[8], Joachim Krautter[9], William Liller[10], David K. Lynch[11,17], Richard J. Rudy[11,17], Steven N. Shore[12,13], Sumner Starrfield[14], and Jim Truran[15,16]

[1] Department of Astronomy, School of Physics and Astronomy, 116 Church Street S.E., University of Minnesota, Minneapolis, MN 55455, USA; ahelton@astro.umn.edu
[2] Department of Physics and Astronomy, Z = 3800, Stony Brook University, Stony Brook, NY, 11794-3800, USA
[3] Department of Geology and Astronomy, West Chester University, 750 South Church Street, West Chester, PA 19383, USA
[4] American Astronomical Society, 2000 Florida Avenue, NW, Suite 400, Washington, DC 20009, USA
[5] Astrophysics Group, Keele University, Keele, Staffordshire ST5 5BG, UK
[6] XMM-Newton Observatory SOC, European Space Astronomy Centre, Apartado 78, 28691 Villanueva de la Canada, Madrid, Spain
[7] Gemini Observatory, 670 North A'ohoku Place, Hilo, HI 96720, USA
[8] NASA Goddard Space Flight Center, Code 665, Greenbelt, MD 20771, USA
[9] Landessternwarte-Zentrum für Astronomie der Universität, Königstuhl, D-69117 Heidelberg, Germany
[10] Institute for Nova Studies, Casilla 5022, Viña del Mar, Chile
[11] The Aerospace Corporation, Mail Stop 2-266, P.O. Box 92957, Los Angeles, CA 90009-2957, USA
[12] Dipartimento di Fisica "Enrico Fermi," Università di Pisa, largo Pontecorvo 3, Pisa 56127, Italy
[13] INFN-Sezione di Pisa, Italy
[14] School of Earth and Space Exploration, Arizona State University, P.O. Box 871404, Tempe, AZ 85287, USA
[15] Department of Astronomy and Astrophysics, University of Chicago, 5640 South Ellis Avenue, Chicago, IL 60637, USA
[16] Argonne National Laboratory, 9700 South Cass Road, Argonne, IL 60439, USA
Received 2010 July 1; accepted 2010 August 26; published 2010 October 14

ABSTRACT

We examine the ejecta evolution of the classical nova V1065 Centauri, constructing a detailed picture of the system based on spectrophotometric observations obtained from 9 to approximately 900 days post-outburst with extensive coverage from optical to mid-infrared wavelengths. We estimate a reddening toward the system of $E(B-V) = 0.5 \pm 0.1$, based upon the $B-V$ color and analysis of the Balmer decrement, and derive a distance estimate of $8.7^{+2.8}_{-2.1}$ kpc. The optical spectral evolution is classified as $P^{o}_{\rm fe}N_{\rm ne}A_{o}$ according to the CTIO Nova Classification system of Williams et al. Photoionization modeling yields absolute abundance values by number, relative to solar of $\rm He/H = 1.6 \pm 0.3$, $\rm N/H = 144 \pm 34$, $\rm O/H = 58 \pm 18$, and $\rm Ne/H = 316 \pm 58$ for the ejecta. We derive an ejected gas mass of $M_g = (1.6 \pm 0.2) \times 10^{-4}\ M_{\odot}$. The infrared excess at late epochs in the evolution of the nova arises from dust condensed in the ejecta composed primarily of silicate grains. We estimate a total dust mass, M_d, of order $(0.2–3.7) \times 10^{-7}\ M_{\odot}$, inferred from modeling the spectral energy distribution observed with the *Spitzer* IRS and Gemini-South GNIRS spectrometers. Based on the speed class, neon abundance, and the predominance of silicate dust, we classify V1065 Cen as an ONe-type classical nova.

Key words: circumstellar matter – novae, cataclysmic variables – stars: individual (V1065 Cen, Nova Cen 2007)

1. INTRODUCTION

Classical novae (CNe) are important contributors to the cycle of chemical enrichment and evolution in galaxies. They violently eject substantial quantities of material that is elementally enriched through explosive nucleosynthesis and through dredge-up from the surface layers of the mass-accreting white dwarf (WD) progenitor. The characteristics of the thermonuclear runaway (TNR) and the subsequent evolution of the nova outburst depend strongly on the mass and composition of the underlying WD. Eruptions on low-mass carbon–oxygen (CO) WDs typically have low expansion velocities, slow light curve evolution, and often, prodigious dust production. In contrast, CNe arising on high-mass ($\gtrsim 1.25\ M_{\odot}$) oxygen–neon (ONe) WDs are generally characterized by high expansion velocities, fast light curve evolution, and little, if any, dust production (Bode & Evans 2008). Novae arising from the latter progenitor frequently are identified by detection of strong [Ne II] $\lambda 12.81\ \mu$m emission. Overall, outbursts on CO WDs are predicted to eject more mass under less energetic conditions than novae on ONe WDs (Schwarz et al. 2007; Townsely & Bildsten 2004). CN energetics may be determined by the speed class, quantified by the parameter t_2, which is the time for the V-band light curve to decline by 2 mag. Faster CNe have higher bolometric (and visual) luminosities at maximum and higher ejection velocities.

More than $10^{-4}\ M_{\odot}$ of material, enriched in CNONeMg and other intermediate-mass elements, can be ejected from the WD at velocities $\gtrsim 10^3$ km s^{-1} as a result of the TNR. As the ejecta disperse, an emission line spectrum is produced and the pseudophotosphere shrinks, revealing a hotter source of emission from stable nuclear burning on the WD surface. CN spectra are remarkable for the temporal development of the ionization states and line profiles present, examination of which is critical for understanding the dynamics of ejection. Low-energy permitted lines of CNO and Fe II give way to He II, as well as highly ionization lines, e.g., [Fe VII] 6087 Å, and in some cases to infrared (IR) "coronal" lines (Lynch et al. 2006, 2008; Woodward et al. 1992, 1997). The latter lines are sources of abundance information since a wide range

[17] Visiting Astronomer at the Infrared Telescope Facility, which is operated by the University of Hawaii under Cooperative Agreement NCC 5-538 with NASA Office of Space Science, Planetary Astronomy Program.

of isoelectronic sequences (e.g., Greenhouse et al. 1990) and adjacent ionization states of metals are observable. As the ejecta cool and evolve, molecules (e.g., Rudy et al. 2003) and dust may form. CNe are often dust-formers and, while amorphous carbon (AC) is a major grain component, silicates, molecules similar to polycyclic aromatic hydrocarbons, and SiC can also be present, occasionally in the same nova (Gehrz 1998).

Many CNe in outburst have exhibited super-soft source (SSS) X-ray spectra (e.g., Ness et al. 2007b). The most likely origin of SSSs is from steady nuclear burning on the surface of a WD (Kahabka & van den Heuvel 1997). One possible fuel source driving this on-going fusion in CNe is from remnant H-rich material left over on the WD surface after the initial mass ejection event. The duration of the SSS, in this case, is expected to be rather short. An alternative fuel source is from continued deposition of material onto the WD surface due to the re-establishment of accretion. This latter mechanism would be able to support a much longer duration SSS stage in post-eruption CN systems. The duration of the SSS phase for Galactic CNe is typically short, only few years, yet a few CNe have been observed to have SSS spectra of much longer duration. V723 Cas, for example, has been an SSS for more than 13 years (Ness et al. 2008).

Here, we discuss synoptic spectrophotometric ground-based and *Spitzer* observations of V1065 Centauri (Nova Cen 2007). The broad temporal and wavelength coverage of our observations affords an opportunity to study the dynamical evolution of this CN, to determine absolute abundances (i.e., metals relative to H), and to infer the physical properties of dust formed in the cooling dense ejecta. The observations of V1065 Cen are discussed in Section 2. Following are discussions of the light curve evolution (Section 3.1), the spectral evolution (Section 3.2), and the reddening and distance estimates (Section 3.3). Photoionization modeling and abundance determinations are presented (Section 4) followed by a discussion of the derived dust properties of V1065 Cen in Section 5. We summarize our conclusions in Section 6.

2. OBSERVATIONS

V1065 Centauri (Nova Cen 2007) was a relatively bright CN outburst first reported by Liller et al. (2007a) at $m_V \simeq 8.2$. A subsequent search of patrol plates revealed a pre-discovery image of the system at $m_V = 7.6 \pm 0.2$ on January 21.04 UT (JD 2,454,121.5) (Liller et al. 2007b). The nova was detected by the "Pi of the Sky" detector (Małek et al. 2010) on January 20.32 UT (JD 2,454,120.8) at an unfiltered magnitude of 6.9. We shall adopt this latter date as day 0 (t_0). Coordinated observations of V1065 Cen commenced shortly after the discovery report and spectrophotometric data were obtained on a variety of facilities including the Small And Moderate Aperture Research System (SMARTS) 1.5 m, the Gemini-South 8 m, the NASA *Spitzer Space Telescope*, and the NASA *Swift* X-ray/UV telescope.[18] Our data span more than 900 days, beginning 9 days after the initial eruption.

2.1. Optical Photometry

The *BVRI* and unfiltered light curves of V1065 Cen obtained from the AAVSO[19] database and from the "Pi of the Sky" project[20] for a period of ∼230 days post-outburst are shown in Figure 1. The vertical tick marks at the top of the panel indicate the dates of our SMARTS, *Spitzer*, and Gemini observations. Three more epochs of *Spitzer* data were obtained beyond the terminus of Figure 1 at days 529, 590, and 763. Also indicated in the figure are three temporal epochs characterized by changes in the observed spectra (Section 3) that delineate different stages in the evolution of V1065 Cen.

The V1065 Cen light curves show a fairly smooth decline after maximum light. They are devoid of secondary maxima and oscillations seen in the light curves of CNe such as V1186 Sco (Schwarz et al. 2007) and V723 Cas (Evans et al. 2003). The most noticeable feature in the early light curve evolution is the dip in the *B* and *V* bands of ∼1 mag near day 40 and the subsequent recovery, a behavior associated with a dust condensation event in the ejecta (Gehrz 2008).

The well-sampled light curves following the decline of V1065 Cen from maximum light enable a determination of the nova's speed class. The optical *BVRI* photometry was fitted using a broken-power-law, $t^{-\alpha}$, relationship using a nonlinear least squares fitting algorithm (the Marquardt method; Bevington & Robinson 1992), which excluded photometry in all bands near the dust formation event (day 40). Figure 2 shows the resultant power-law fits. The derived early light decline rates (prior to day 90) were $\alpha = 0.99 \pm 0.01$, 1.10 ± 0.01, 1.04 ± 0.01, and 1.28 ± 0.01 for *B*, *V*, *R*, and *I* bands, respectively. At later dates ($\gtrsim$day 90) $\alpha = 2.33 \pm 0.01$, 1.90 ± 0.01, 3.12 ± 0.01, and 2.96 ± 0.01. The time for the *V*-band light curve to decline 2 mag, t_2, and 3 mag, t_3, are ∼11 days and ∼26 days, respectively. The decay time calculated from the unfiltered "Pi of the Sky" data was in excellent agreement, $t_2 \sim 11$. These values are commensurate with the "fast" speed class of CNe (Payne-Gaposchkin 1957; Duerbeck 2008), similar to V382 Vel (Shore et al. 2003). Novae in this speed class are typically believed to arise on massive WDs (Gehrz et al. 1998).

2.2. Optical Spectroscopy

V1065 Cen was observed using the R-C Spectrograph on the 1.5 m telescope operated by the SMARTS (Small and Moderate Aperture Research Telescope System) Consortium at the Cerro Tololo Inter-American Observatory (CTIO) as part of the Stony Brook Nova program (Table 1). The data were obtained using four different instrumental setups. The low-resolution blue (*B*) setup used a 600 lines mm^{-1} grating with a resolution of 4.1 Å pixel^{-1} ($\lambda/\Delta\lambda = R \sim 1200$) and spectral coverage of 3650–5400 Å. The high-resolution blue (*B*2) setup achieved a 1.6 Å pixel^{-1} resolution ($R \sim 2600$) over two bandpasses, 3870–4540 Å and 4050–4700 Å, with an 831 lines mm^{-1} grating at second order. The red portion of the spectrum was observed at low resolution (3.1 Å pixel^{-1}; $R \sim 2000$) with the grating positioned at first order with coverage of 5650–6950 Å. The long-wavelength red (*R*2) setup covered the range 6000–9000 Å at a resolution of 6.5 Å pixel^{-1} ($R \sim 1200$). The low-resolution data were observed with a 1.″1 slit while the high-resolution observations utilized a 0.″83 slit width.

The data were reduced in IDL using standard optical spectral data reduction procedures, as described on the Stony Brook SMARTS Nova Atlas Web site.[21] For each set of observations, three images were obtained and median combined to remove cosmic rays. Wavelength calibration was performed using

[18] All spectroscopic data presented in the figures in this paper are provided online at http://www.astro.sunysb.edu/fwalter/SMARTS/NovaAtlas/v1065cen/data/index.html.

[19] http://www.aavso.org

[20] http://grb.fuw.edu.pl/

[21] http://www.astro.sunysb.edu/fwalter/SMARTS/NovaAtlas/atlas_spec.html

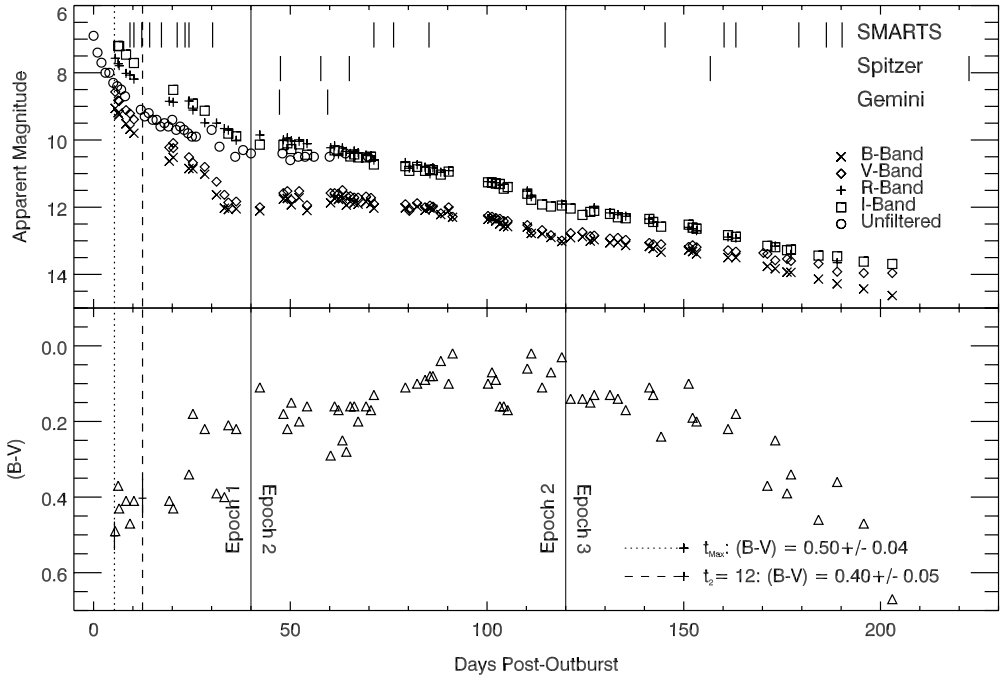

Figure 1. Light curve of V1065 Cen. Top: the *BVRI*-band photometry is taken from the AAVSO database while the unfiltered photometry is taken from the "Pi of the Sky" project data. Vertical tick marks delineate dates of the SMARTS, *Spitzer*, and Gemini observations (Section 2). Bottom: the $(B-V)$ color of V1065 Cen is derived from the AAVSO photometry.

Th–Ar or Ne calibration lamps. Only a single spectrophotometric standard was observed each night, typically LTT 4364 or Feige 110. Thus, slit losses, changes in seeing, and sky transparency permit only approximate flux calibration. Differences in airmass between the target and the standard may have resulted in small wavelength-dependent offsets, but we expect this to have only a minimal impact on the continuum shape. To determine the flux in the emission lines, a nonlinear least squares Gaussian fitting routine was used that fit the line center, line amplitude, line width, continuum amplitude, and the slope of the continuum. Selected SMARTS optical spectra are presented in Figure 3. A summary of identified lines and the measured line fluxes (in units of 10^{-12} erg s^{-1} cm^{-2}), uncorrected for reddening, is collated in Table 2.

2.3. Near-IR Spectroscopy

Near-IR spectra of V1065 Cen were obtained at Gemini-South with the Gemini Near Infra-Red Spectrograph (GNIRS; Elias et al. 2006) on 2007 March 08.22 UT (JD 2,454,167.72; day 47) and 2007 March 20.2 UT (JD 2,454,179.69; day 59) as part of a queue nova target of opportunity program GS-2007A-Q-25. The first GNIRS observations were obtained soon after the *V*-band light curve resumed its smooth decline after recovery from the initial dust extinction event (Section 5). Spectra were obtained in cross-dispersed mode (XD) using a $0\farcs45 \times 6\farcs1$ slit (~3 pixels in width) and the 31.7 line mm^{-1} grating, providing spectral coverage from 0.9 to 2.5 μm with a resolution of $R = 1700$. Due to target brightness, multiple exposure strategies were attempted to prevent saturation of emission lines. Unsaturated exposure sequences included 20 coadded 1.0 s exposures (20×1.0), 80×1.0, and 40×2.0. For the final analysis, all unsaturated data were combined. Acquisition images obtained with the H_2 filter ($\lambda_o = 2.122$ μm) were saturated preventing their use as reliable flux points.

The data were reduced using the Gemini IRAF[22] package v1.9.1 (2006 December 20) following the methodology described on the Gemini Data Documentation page.[23] Wavelength calibration was established using arc-lamp spectra. The telluric calibration star, HIP 59084, exhibited strong hydrogen absorption lines in its spectrum, requiring interpolation of the continuum across the stronger absorption features. Regions of the spectra near Pa ϵ (0.955 μm), Br 13 (1.611 μm), and Br 15 (1.57 μm) were blended with telluric features preventing rectification. The standard HIP 53285 was used for flux calibration.

Prominent emission lines in the GNIRS spectra were fitted in a manner similar to that described for the optical spectra (Section 2.2). The GNIRS spectra are shown in Figure 4, while line identification and the measured line fluxes (in units of 10^{-12} erg s^{-1} cm^{-2}), uncorrected for reddening, are summarized in Table 3.

2.4. Spitzer Spectroscopy

V1065 Cen was observed on six dates with the NASA *Spitzer Space Telescope* (*Spitzer;* Gehrz et al. 2007; Werner et al. 2004) using the IRS (Houck et al. 2004) as part of our long-term *Spitzer* CNe study conducted over multiple *Spitzer* cycles. A summary of the *Spitzer* observations conducted under various program identification numbers (PIDs) is provided in Table 4. Spectra were obtained using all modules of the IRS. The resolving power of the low-resolution modules, i.e., the short wavelength (5.2–14.5 μm) low-resolution module (SL) and the long-wavelength (14.0–38.5 μm) low-resolution module (LL), is $R = \lambda/\Delta\lambda \sim 60$–$128$. $R \sim 600$ for the high-resolution modules, the short wavelength (9.9–19.5 μm) high-resolution module (SH) and long-wavelength (18.7–37.2 μm)

[22] IRAF is distributed by the National Optical Astronomy Observatory, which is operated by the Association of Universities for Research in Astronomy, Inc., under cooperative agreement with the National Science Foundation.
[23] http://www.gemini.edu/sciops/data/dataIndex.html

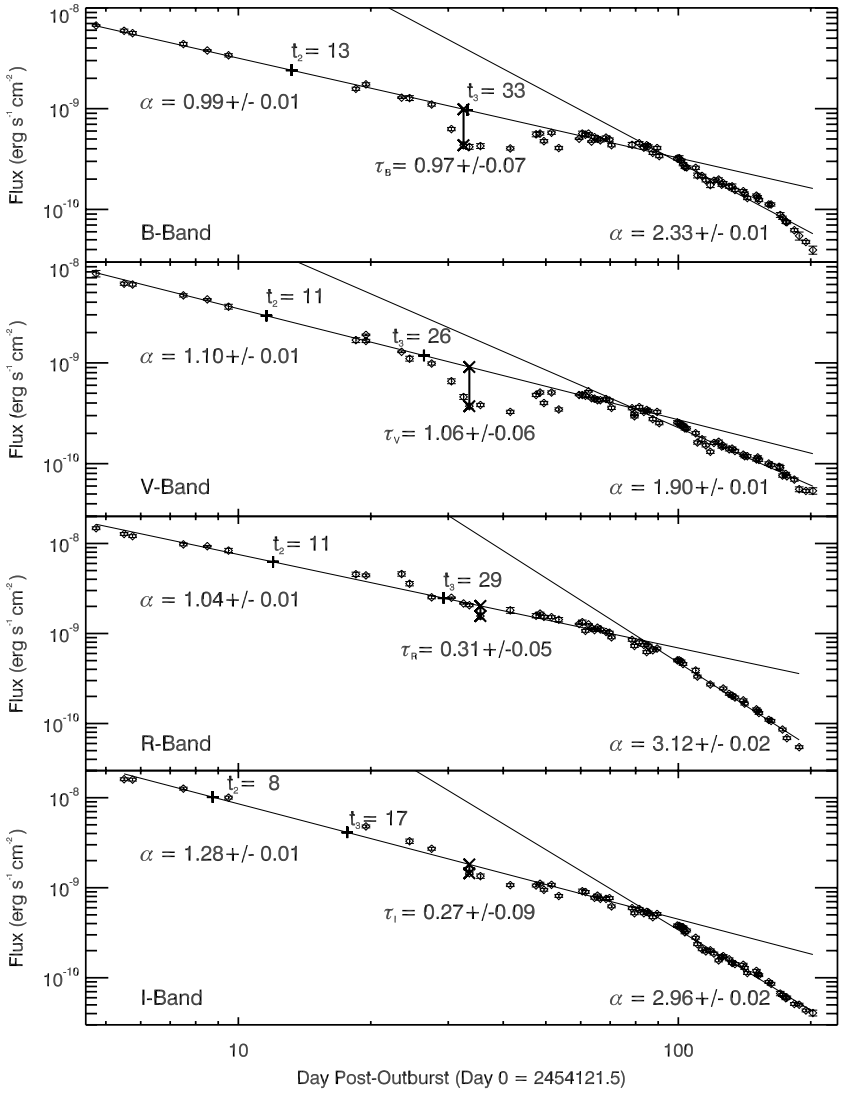

Figure 2. Power-law behavior of the V1065 Cen *BVRI* light curves. The fluxes are derived from photometry in the AAVSO database and the solid lines indicate the $t^{-\alpha}$ power-law fit where the best-fit value of α is indicated. The time to decline 2 mag, t_2, and 3 mag, t_3, from maximum light are labeled (cross), while the optical depth, τ_λ, of the dust extinction event maximum in each photometric band is also indicated.

high-resolution module (LH). Emission lines observed in V1065 Cen with the latter modules are resolved. All observations utilized blue (13.3–18.7 μm) IRS peak-up "on source" to ensure proper placement of the target in the narrow IRS slits.

IRS basic calibrated data (BCD) products from the first three visits (Table 4) were calibrated and processed with the *Spitzer* Science Center (SSC) IRS pipeline v16.1.0 for the short–low (SL) module and v15.3.0 for all other modules. BCDs generated from all IRS modules for the last two target visits were processed entirely with pipeline version v16.1.0. Details of the calibration and raw data processing are specified in the IRS Pipeline Description Document.[24] Bad pixels in individual BCDs were identified using bad pixel masks provided by the SSC and corrected using a linear interpolation. Multiple data collection events were obtained at two different positions on the slit using *Spitzer*'s nod functionality for the low-resolution modules, which enabled differencing of the two-dimensional SL and LL BCDs to remove the background flux contribution. For SH and LH BCDs, adjacent follow-on observations of "blank-fields" were averaged together to create two-dimensional sky images that were then subtracted from each on-source BCD. Spectra were then extracted from the background corrected BCDs using Spice (v1.4.1) with the default point source extraction widths. The extracted spectra were then combined using a weighted linear mean into single output data files with the standard deviations of the flux at each wavelength bin providing an estimate for the uncertainty in the observed flux. Since no appreciable fringing was detected in the IRS data, the spectra were not defringed. Emission line fluxes were measured as described in Section 2.2.

The *Spitzer* IRS data are shown in Figures 5–7. Table 5 summarizes the line identifications and the measured line fluxes (in units of 10^{-13} erg s^{-1} cm^{-2}), uncorrected for reddening.

2.5. X-ray and Ultraviolet Observations

More than two years after outburst (t_0), V1065 Cen was observed three times with *Swift*, on 2009 February 5.7, February 14.1, and July 11.0 UT, corresponding to days 746.7, 755.3, and 902.4 after outburst. Data acquisition, reduction, and analysis followed the methods presented by Ness et al. (2007a). The exposure times were 2.15, 2.40, and 4.95 ks and yielded only

[24] Version 1.0; http://ssc.spitzer.caltech.edu/irs/dh/

Table 1
Ground-based Spectroscopic Observing Log

Observation Date	JD (+2,450,000)	Band[a]	Exposure Time (s)	Age[b] (days)
SMARTS-Epoch 1				
2007 Jan 29.29	4129.79	*R*	180	8.97
2007 Jan 29.34	4129.84	*B*2	600	9.02
2007 Jan 30.24	4130.74	*B*	300	9.92
2007 Jan 31.24	4131.74	*R*	180	10.92
2007 Jan 31.29	4131.79	*B*2	600	10.97
2007 Feb 01.27	4132.77	*B*	360	11.95
2007 Feb 02.25	4133.75	*R*	150	12.93
2007 Feb 02.33	4133.83	*B*2	600	13.01
2007 Feb 04.28	4135.78	*R*	150	14.96
2007 Feb 04.35	4135.85	*B*2	600	15.03
2007 Feb 05.21	4136.71	*B*	450	15.89
2007 Feb 06.21	4137.71	*B*2[c]	150	16.89
2007 Feb 06.30	4137.80	*R*	150	16.98
2007 Feb 07.21	4138.71	*B*	540	17.89
2007 Feb 09.20	4140.70	*B*	720	19.88
2007 Feb 10.13	4141.63	*B*2[c]	900	20.81
2007 Feb 10.23	4141.73	*R*	150	20.91
2007 Feb 10.25	4141.75	*B*2	1200	20.93
2007 Feb 11.29	4142.79	*R*2	300	21.97
2007 Feb 12.20	4143.70	*B*	600	22.88
2007 Feb 13.10	4144.60	*B*2[c]	1200	23.78
2007 Feb 13.21	4144.71	*R*	180	23.89
2007 Feb 13.36	4144.86	*B*2	1200	24.04
2007 Feb 14.17	4145.67	*B*	600	24.85
2007 Feb 18.14	4149.64	*B*	600	28.82
2007 Feb 22.17	4153.67	*B*2	1200	32.85
Epoch 2				
2007 Mar 31.16	4190.66	*B*	1200	69.84
2007 Apr 01.29	4191.79	*R*	540	70.97
2007 Apr 02.12	4192.62	*R*	540	71.80
2007 Apr 06.14	4196.64	*B*	1200	75.82
2007 Apr 07.11	4197.61	*R*	720	76.79
2007 Apr 09.10	4199.60	*R*2	300	78.78
2007 Apr 12.12	4202.62	*B*	1200	81.80
2007 Apr 19.18	4209.68	*R*	540	88.86
Epoch 3				
2007 Jun 09.99	4261.49	*R*2[d]	900	140.67
2007 Jun 22.01	4273.51	*B*	1800	152.69
2007 Jun 28.00	4279.50	*B*	1200	158.68
2007 Jun 28.97	4280.47	*B*2	1200	159.65
2007 Jun 29.97	4281.47	*R*	540	160.65
2007 Jun 30.95	4282.45	*B*2	1200	161.63
2007 Jul 02.08	4283.58	*B*	1200	162.76
2007 Jul 03.96	4285.46	*B*2	1200	164.64
2007 Jul 17.96	4299.46	*R*2	900	178.64
2007 Jul 18.99	4300.49	*B*	1200	179.67
2007 Jul 25.07	4306.57	*B*	900	185.75
2007 Jul 25.96	4307.46	*B*2	1800	186.64
2007 Jul 28.96	4310.46	*B*	1200	189.64
2007 Jul 30.96	4312.46	*B*2	1800	191.64
2009 Jun 07.21	4338.71	*R*	1200	717.89
2009 Jun 08.24	4834.74	*B*	1800	718.92
Gemini-South Epoch 2				
2007 Mar 08.14	4167.63	SC/XD[e]	80	46.81
2007 Mar 20.16	4179.65	SC/XD	80	58.83

Notes.
[a] Spectral ranges are 0.365–0.540 μm for *B* band, 0.405–0.470 μm for *B*2 band, 0.565–0.695 μm for *R* band, and 0.622–0.886 μm for *R*2 band, unless specified otherwise.
[b] From 2007 Jan 20.32 (JD 2,454,120.82).
[c] Spectral range is 0.387–0.454 μm.
[d] Spectral range is 0.544–0.808 μm.
[e] Spectral range is 0.88–2.50 μm.

marginal detections with $(1.5 \pm 1.2) \times 10^{-3}$, $(1.2 \pm 1.1) \times 10^{-3}$, and $(0.8 \pm 0.6) \times 10^{-3}$ counts s^{-1}, respectively. Errors quoted are 1σ errors calculated using likelihood statistics (Ness et al. 2007a). Not enough events were recorded to characterize the X-ray spectrum. The X-ray observations clearly indicate low activity likely from the accretion disk or X-ray line emission. With no significant soft X-rays detected, the data strongly imply that nuclear burning on the WD surface ended well before the observations were taken. This suggests that if V1065 Cen underwent a SSS stage, it was less than two years in duration.

Swift UV filter magnitudes were obtained simultaneously with the X-ray observations. In the *uvw*2 filter (1928 Å), the magnitude evolved from 17.98 ± 0.07 to 18.23 ± 0.07 between days 746.7 and 755.3. In the *uvm*2 bandpass (2246 Å), the magnitudes were 18.31 ± 0.10, 18.14 ± 0.09, and 18.76 ± 0.13, and in the *uvw*1 filter (2600 Å), the magnitudes were 17.52 ± 0.05, 17.77 ± 0.07, and 18.10 ± 0.04 observed on days 746.7, 755.3, and 902.4, respectively.

3. DISCUSSION

3.1. Light Curve Evolution

Ennis et al. (1977) used a fixed mass, optically thin, expanding spherical shell model to fit the light curve of the fast nova V1500 Cyg (Nova Cygni 1975), assuming emission from a free–free continuum. They described the light curve decline by the relationship

$$F_\lambda \propto t^{-2} \left(1 + \frac{2c_s t}{H}\right)^{-1}, \quad (1)$$

where H is the initial shell thickness, c_s is the sound speed in the plasma, and t is the number of days since outburst. This model predicts that the flux will decline as t^{-2} at early times with a transition to a t^{-3} power-law decline at later epochs.

The trend in the early light curves (Figure 2) of V1065 Cen deviates strongly from that predicted by Ennis et al. (1977). Instead, we find that the early light curve decline is $\propto t^{-1}$. One possible cause of the observed divergence from the theoretical light curve behavior is the presence of strong emission lines. Early in the evolution, the spectra are dominated by Fe II. As the system evolves, emission by [O III] λλ4959, 5007 begins to dominate the spectra near 5000 Å (Figure 3). In order to determine the contribution to the light curve by the continuum alone, we combined those blue and red SMARTS spectra that were observed nearly simultaneously, providing 10 data points covering the first 160 days after outburst. We interpolated across the emission lines and the gap between the two spectral regions to isolate the continuum contribution to the visual photometric bandpass. We fitted the rectified photometry and found a decay rate $\propto t^{-1.4}$. Though there were large uncertainties in fitting the continuum and, hence, in determining the decay rate of the continuum alone, the derived rate of decline still suggests that emission line intensities have a significant impact on the decay rate of the light curve, but are not entirely sufficient to explain the light curve behavior. This supports the conclusion that the system is not well characterized by a simple, homogeneous, expanding shell model.

A break in the decay rate is evident near day 90 (Figure 2). Power-law fits to the decline rates after the break at *B* and *V* bands are $\propto t^{-2}$, while for the redder passbands, the decay rate is $\propto t^{-3}$. This behavior is more consistent with the expanding optically thin shell model of Ennis et al.

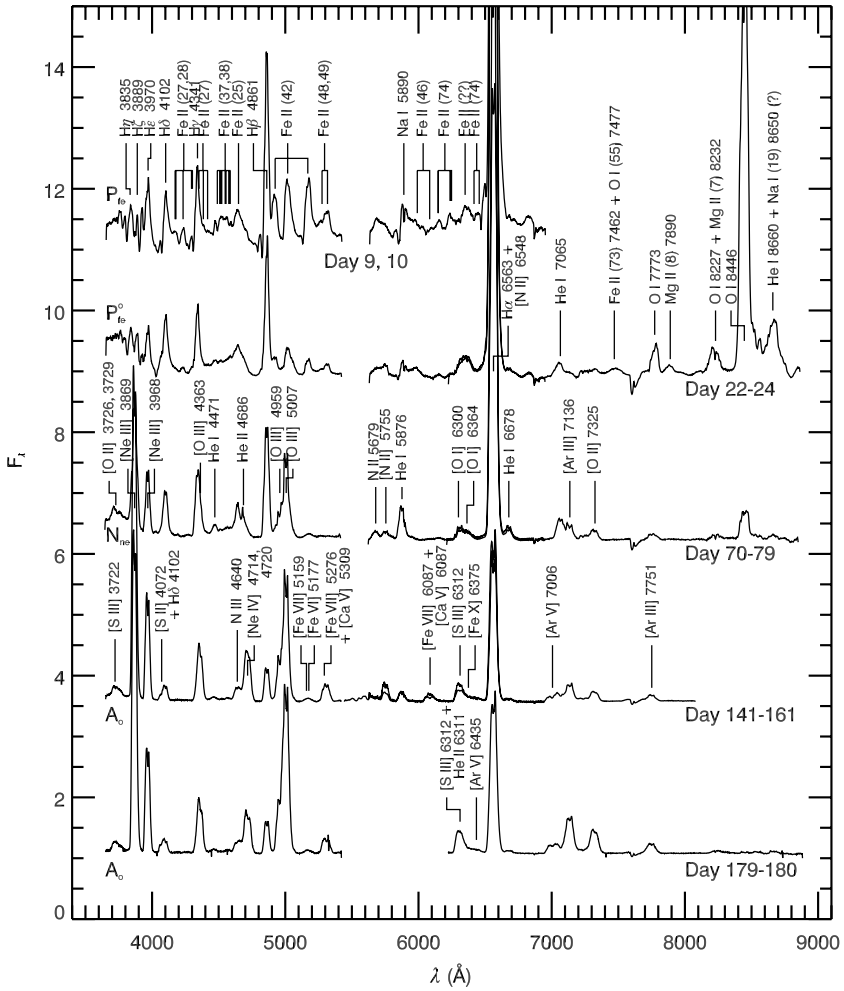

Figure 3. Evolution of the optical spectrum on V1065 Cen. The spectra have been arbitrarily scaled and prominent features labeled. The associated spectral evolutionary phase ($P^o_{\rm fe}$, $N_{\rm ne}$, A_o) for each epoch is listed to the left of the spectra.

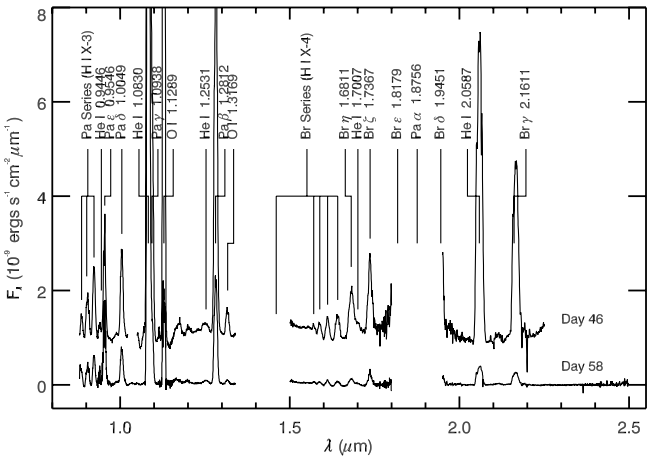

Figure 4. Evolution of the near-infrared spectrum of V1065 Cen. The spectra have been arbitrarily scaled and prominent features labeled. The breaks in the SED are due to roll-off of the eschelle orders and telluric contamination.

3.2. Spectral Evolution

A typical CN at maximum light has an optical spectrum resembling that of an F-type supergiant with strong neutral lines of O I, C I, Fe II, and Mg I coexisting alongside the H I recombination spectrum. In some cases, Na I emission is also observed at this stage. This "principal" spectrum lasts until the light curve has declined by $\simeq$3.5 mag. As the pseudophotosphere recedes and the ejecta densities decline, the optical spectrum transitions into the "diffuse-enhanced" spectrum, during which strong Fe II and O I lines persist. Both early stages of development are characterized by P-Cygni profiles that often exhibit complex, multi-component absorption features (Williams 1994). The declining optical depth of the expanding ejecta, eventually leads to the appearance of the "nebular" spectrum during which forbidden transitions dominate. Optical spectra at this later stage include forbidden lines of [N I], [N II], and [O I–III]. Some CNe go on to exhibit "coronal" emission (Greenhouse et al. 1990) from highly ionized species of Ne, Mg, and Fe. A more complete discussion of the spectral development of CNe is provided by Hack et al. (1993), Williams et al. (1991), and Williams (1992). We obtained optical and nearly contemporaneous IR observations of V1065 Cen throughout much of this development.

3.2.1. Epoch 1 (E1)—Principal and Diffuse-enhanced Spectra

The initial principal spectrum (Figure 3) was dominated by hydrogen Balmer series emission including Hα and going beyond Hη. Higher order transitions rapidly blended into the Balmer continuum at short wavelengths. Near day 9, Hα had a FWHM expansion velocity of nearly 3000 km s^{-1} while Hβ and Hγ were nearer to 1200 km s^{-1} due to suppression of the line wings from P-Cygni absorption. Within days, all these strong H-recombination lines were observed to have FWHM velocities

Table 2
Line Identifications and Fluxes from Smarts Optical Spectra[a]

Identification	Epoch 1		Epoch 2	Epoch 3	
	2007 Jan 29[b] (Days 9, 10)	2007 Feb 11 (Days 22–24)	2007 Mar 31 (Days 70, 71, 79)	2007 Jun 10 (Days 141, 159, 161)	2007 Jul 18 (Days 179, 190)
[O II]λ3738 + [Fe VII]λ3738	...	...	...	2.75 ± 0.02	1.49 ± 0.01
H(10) λ3798	1.46 ± 0.06	1.25 ± 0.06	...	...	...
Hηλ3835	9.68 ± 0.16	7.57 ± 0.08	...	...	...
[Ne III]λ3869	...	...	16.3 ± 0.07	20.8 ± 0.01	7.70 ± 0.00
Hζλ3889	8.19 ± 0.09	6.19 ± 0.07	...	...	...
[Ne III]λ3967+ Heλ3970	...	...	6.15 ± 0.07	6.80 ± 0.01	2.68 ± 0.00
Heλ3970	14.0 ± 0.10	12.7 ± 0.08	...	...	...
Hδλ4102	4.73 ± 0.08	17.1 ± 0.08	5.74 ± 0.08	1.44 ± 0.01	0.75 ± 0.01
Fe II (27) λ4173+ Fe II (28) λ4179	17.9 ± 0.15	...	...	...	...
Fe II (27) λ4233	17.7 ± 0.14	0.16 ± 0.03	...	...	...
Hγλ4341+ Fe II (27) λ4352	12.4 ± 0.10	18.7 ± 0.07	9.90 ± 0.08	...	...
[O III]λ4363	...	...	...	4.37 ± 0.01	1.22 ± 0.00
He I λ4471	...	...	0.61 ± 0.07	0.83 ± 0.02	1.40 ± 0.02
Fe II (37) λ(4491 + 4489)	6.42 ± 0.09	4.70 ± 0.22	...	...	...
Fe II (37) λ(4515 + 4520)+ Fe II (38) λ(4523 + 4508)	20.2 ± 0.31	2.60 ± 0.26	...	...	...
Fe II (37) λ4555+Fe II (38) λ4549	18.7 ± 0.29	...	0.57 ± 0.29	...	...
Fe II (26) λ4584+Fe II (37) λ4583+ Fe II (38) λ(4576 + 4584)	3.65 ± 0.10	4.16 ± 0.23	...	...	...
N III λ4640	...	...	2.91 ± 0.10	1.26 ± 0.01	0.33 ± 0.00
Fe II (25) λ4649	68.1 ± 0.42	17.0 ± 0.19	...	...	...
[Ne IV]λ(4714 + 4720)	...	...	...	4.84 ± 0.01	1.22 ± 0.01
Hβλ4861	29.2 ± 0.14	36.3 ± 0.08	15.3 ± 0.07	2.37 ± 0.01	0.85 ± 0.00
Fe II (42) λ4924	27.5 ± 0.12	5.76 ± 0.09	...	...	...
[O III]λ4959	...	...	2.96 ± 0.11	2.13 ± 0.01	0.83 ± 0.00
[O III]λ5007	...	...	13.1 ± 0.12	10.7 ± 0.01	5.82 ± 0.01
Fe II (42) λ5014	67.5 ± 0.23	11.1 ± 0.09	...	...	...
[Fe VII]λ5159 + [Fe VI]λ5176	...	...	...	0.23 ± 0.01	0.14 ± 0.00
Fe II (42) λ5174	45.4 ± 0.17	4.39 ± 0.08	0.33 ± 0.07	...	...
Fe II (49) λ5276	14.7 ± 0.37	1.38 ± 0.09	...	...	...
[Ca V]λ5309 + [Fe VII]λ5276	...	...	...	1.63 ± 0.01	0.48 ± 0.00
Fe II (49) λ5317	13.3 ± 0.22	2.90 ± 0.05	...	...	×[c]
N II λ5679	27.4 ± 0.02	4.16 ± 0.01	1.58 ± 0.01	...	×
[N II]λ5755 + [Fe VII]λ5738	...	...	...	1.60 ± 0.07	×
[N II]λ5755	14.0 ± 0.02	3.48 ± 0.01	2.14 ± 0.2	...	×
He I λ5876	...	...	5.62 ± 0.01	0.82 ± 0.05	×
Na I λ5890	42.7 ± 0.02	6.46 ± 0.02	...	...	×
Fe II (46) λ6084	10.6 ± 0.02	...	...	...	×
[Ca V]λ6087 + [Fe VII]λ6087	...	...	...	0.92 ± 0.05	×
Fe II (74) λ(6148 + 6149)	13.1 ± 0.02	2.08 ± 0.01	0.36 ± 0.01	...	×
Fe II (74) λ(6248 + 6238)	10.8 ± 0.01	1.54 ± 0.01	...	...	×
Fe II (??) λ6315	26.1 ± 0.03	25.0 ± 0.02	...	...	×
[O I]λ6300 + [S III]λ6312	...	...	1.42 ± 0.02	1.79 ± 0.06	×
[O I]λ6364	...	...	2.66 ± 0.02	1.03 ± 0.09	×
Hαλ6563 + [N II]λ6548	908 ± 0.02	442 ± 0.01	106 ± 0.01	14.7 ± 0.04	×
He I λ6678	1.09 ± 0.02	2.11 ± 0.01	2.54 ± 0.01	0.36 ± 0.05	×
[Ar V]λ7007	×	15.4 ± 0.1	...	0.25 ± 0.00	0.24 ± 0.01
He I λ7067	×	...	4.14 ± 0.03	0.86 ± 0.00	0.51 ± 0.02
[Ar III]λ7136	×	...	2.54 ± 0.03	1.91 ± 0.01	2.18 ± 0.01
[Ar IV]λ7236	×	...	...	0.31 ± 0.00	0.17 ± 0.01
He I λ7281	×	10.7 ± 0.1	2.10 ± 0.04	...	...
[O II]λ7325 + [Ca II]λ7324	×	...	...	1.09 ± 0.00	1.36 ± 0.01
Fe II (73) λ7462	×	10.9 ± 0.1	...	...	...
He II λ7593	×	...	...	0.05 ± 0.00	0.004 ± 0.001
[Ar III]λ7751	×	...	...	0.81 ± 0.00	0.67 ± 0.01
[Ar III]λ7751+ O I λ7773	×	...	1.19 ± 0.02	...	...
O I λ7773	×	27.1 ± 0.1	...	...	...
Mg II (8)λ7890	×	9.02 ± 0.10	...	×	...
O I λ8227	×	34.2 ± 0.1	...	×	...
O I λ8227+ He II λ8239	×	...	1.06 ± 0.03	×	0.30 ± 0.01
O I λ8446	×	453.6 ± 0.3	6.13 ± 0.04	×	0.13 ± 0.01
He I λ8653+ He I λ8665	×	86.7 ± 0.2	0.91 ± 0.03	×	0.14 ± 0.01

Notes.
[a] Flux values are in units of 10^{-12} erg s^{-1} cm^{-2}.
[b] For observations spanning multiple days, this marks the first observation in the series.
[c] For entries with a × the data does not extend to that wavelength.

Table 3
Line Identifications and Fluxes from GNIRS Near-IR Spectra—Epoch 2

Identification	2007 Mar 8[a]	2007 Mar 20
Pa(11) λ0.8863	7.53 ± 1.52	3.84 ± 0.24
Paηλ0.9015 + [S III]λ0.9069[b]	12.2 ± 0.6	8.23 ± 0.10
Paζλ0.9229[b]	13.0 ± 0.3	6.81 ± 0.06
He I? λ0.9466[b]	3.33 ± 0.3	1.68 ± 0.05
Paελ0.9546 + [S III]λ0.9532	18.6 ± 1.8	12.7 ± 0.06
Paδλ1.0049	16.8 ± 0.2	7.29 ± 0.06
He I λ1.0830	417.3 ± 0.5	179 ± 0.03
Paγλ1.0938	44.8 ± 0.5	9.31 ± 0.03
O I λ1.1289	104.6 ± 0.4	17.2 ± 0.02
C I? λ1.1600–1.1800	13.7 ± 0.8	...
N I?, C I? λ1.2074; 1.2088	11.2 ± 1.3	...
He I λ1.2531	2.90 ± 0.31	1.56 ± 0.03
Paβλ1.2818	87.9 ± 0.2	24.1 ± 0.02
O I λ1.3169	6.87 ± 0.26	3.08 ± 0.04
Br(15) λ1.5705 (?)	...	0.40 ± 0.02
Br(14) λ1.5884	...	0.54 ± 0.02
Br(13) λ1.6114	2.16 ± 0.32	1.09 ± 0.02
Br(12) λ1.6412	6.44 ± 0.32[c]	1.37 ± 0.02
Brηλ1.6811	...	2.59 ± 0.03
He I λ1.7007	15.4 ± 0.5	0.87 ± 0.02
Brζλ1.7367	...	3.27 ± 0.02
C I? λ1.7662	17.5 ± 0.4	...
He I λ2.0587	111.1 ± 5.4	6.28 ± 0.04
Brγλ2.1661	68.1 ± 5.7	4.49 ± 0.04

Notes.
[a] Flux values are in units of 10^{-12} erg s^{-1} cm^{-2}.
[b] Weighted average of eschelle orders 7 and 8.
[c] Weighted average of eschelle orders 4 and 5.

of 2000–2500 km s^{-1}, with no indication of deceleration for the next 130 days, at which point the lines became blended with other emission lines from metals. The consistency of the expansion velocity inferred from the FWHM measurements as the line flux declined suggests that the primary source of emission was a distinct, thin shell with a weak velocity gradient rather than a thick shell with a high velocity gradient (Shore et al. 1993).

Fe II multiplet emission was also prominent during the early epochs. Of these, only the Fe II (42) lines were distinct and strong enough to obtain unambiguous line fits. These lines had FWHM velocity widths between 2700 and 3900 km s^{-1} (HWZI ∼ 4650–6750 km s^{-1}). The high expansion velocity of the iron lines resulted in a blending of the numerous other multiplet lines (e.g., 27, 28, 37, 38), explaining the complicated structure of the continuum and the many broad, complex features such as those observed near 4350–4800 Å. We classify V1065 Cen as an "Fe II"-type nova due to the predominance of strong iron emission at early epochs and suggest that it is a member of the "broad" subclass since the HWZI line widths exceeded 2500 km s^{-1} (Williams et al. 1994). No other non-Balmer emission lines were of comparable brightness at this epoch, which implies a spectral evolutionary stage of $P_{\rm fe}$ using the CTIO classification system (Williams et al. 1991, 1994).

Na I D was observed in emission with a single very strong P-Cygni absorption component. Interstellar sodium absorption lines were in evidence near the rest wavelength (Section 3.3). Observations from days 9 and 10 exhibited a broad complex near 5700 Å possibly due in part to N II λ5679. As this feature evolved, its individual components became more distinct, eventually resolving into N II λ5679 and [N II] λ5755 (see Section 3.2.2).

Initial observations showed a complex around 6330 Å that we tentatively attribute to Fe II. As the ejecta thins, this complex broadened and strengthened relative to the continuum. In other "Fe II"-type novae, this region frequently gives rise to emission from [O I] λλ6300, 6364 ($^1D_2$–$^3P_2$ and $^1D_2$–$^3P_1$, respectively; Williams 1994). The attribution to [O I] at this epoch is not straightforward, however. Based upon the transition probabilities alone, one expects a roughly 3:1 line ratio. The high expansion velocities observed in the ejecta would blend the doublet together, but the resulting structure should be asymmetrical. Instead, the observed structure at day 22 is quite smooth and symmetric. At this stage, a correct identification is elusive.

Observations obtained on day 22 extended to nearly 9000 Å. These spectra revealed additional permitted emission from He I λ7065, λ8660, O I λ7773, λ8227, λ8446, and possible multiplet emission from Mg II at λ7890 and λ8232. Of particular interest in these data are the O I lines. O I λ8446 was the strongest non-Balmer line in the spectrum followed by O I λ7773 (see Section 3.2.2). Due to the presence of O I λ8446 at a strength greater than Hβ, we classify this stage of development as $P^o_{\rm fe}$.

Both the Balmer lines and the isolated Fe II (42) lines in the principal spectrum had asymmetrical profiles due to strong P-Cyg absorption with multiple complex components (Figure 8). Initially there were two dominant P-Cyg absorption components. The higher velocity component was ∼−4250 km s^{-1} for each Balmer line. The lower velocity component was ∼−2500 km s^{-1} for Hα but nearer to ∼−2250 km s^{-1} for the other Balmer transitions. Absorption by the high velocity component rapidly disappeared while the signature of the low-velocity component remained for at least the first 30 days after outburst, disappearing completely near day 60. Around day 10 a third weak P-Cygni absorption component was clearly evident in the high resolution spectra at velocities of ∼−1650 km s^{-1}. The strength of this third component remained fairly constant as the absorption depth from other components diminished. The absorption minima near the Fe II (42) lines had velocities between −900 and −1450 km s^{-1} and, thus, were likely due to the material producing the low-velocity P-Cygni absorption observed in the Balmer lines.

P-Cygni absorption profiles in CNe are often interpreted as arising in a shell of material ejected at high velocities during the initial TNR. Understanding the clumpiness and the morphology of these ejecta is useful to constrain photoionization model assumptions. In V1065 Cen, there were three distinct absorption components with behavior similar to the evolution observed in other CN systems (e.g., V603 Aql; McLaughlin 1960). Observations of V1974 Cyg revealed two distinct absorption components that Shore et al. (1993) attributed to a high-velocity polar outflow along with a low-velocity equatorial wind. Woodward et al. (1997), in their analysis of early observations of V1974 Cyg, argued that initially there was a P-Cygni absorption component that was much slower than the full-width zero intensity of prominent hydrogen emission lines. These latter P-Cygni components were accelerated by ∼700 km s^{-1} as the nova evolved and were interpreted to be evidence of high-density optically thick clumps ejected by an early slow wind. Following the arguments of Shore et al. (1993) and Woodward et al. (1997), the high-velocity P-Cygni absorption component (−4250 km s^{-1}) in V1065 Cen could be attributed to polar plumes of ejecta and the low-velocity components to an equatorial wind.

Alternatively, in a study of resolved nova shells, Slavin et al. (1995) found that those CNe classified as "fast" novae

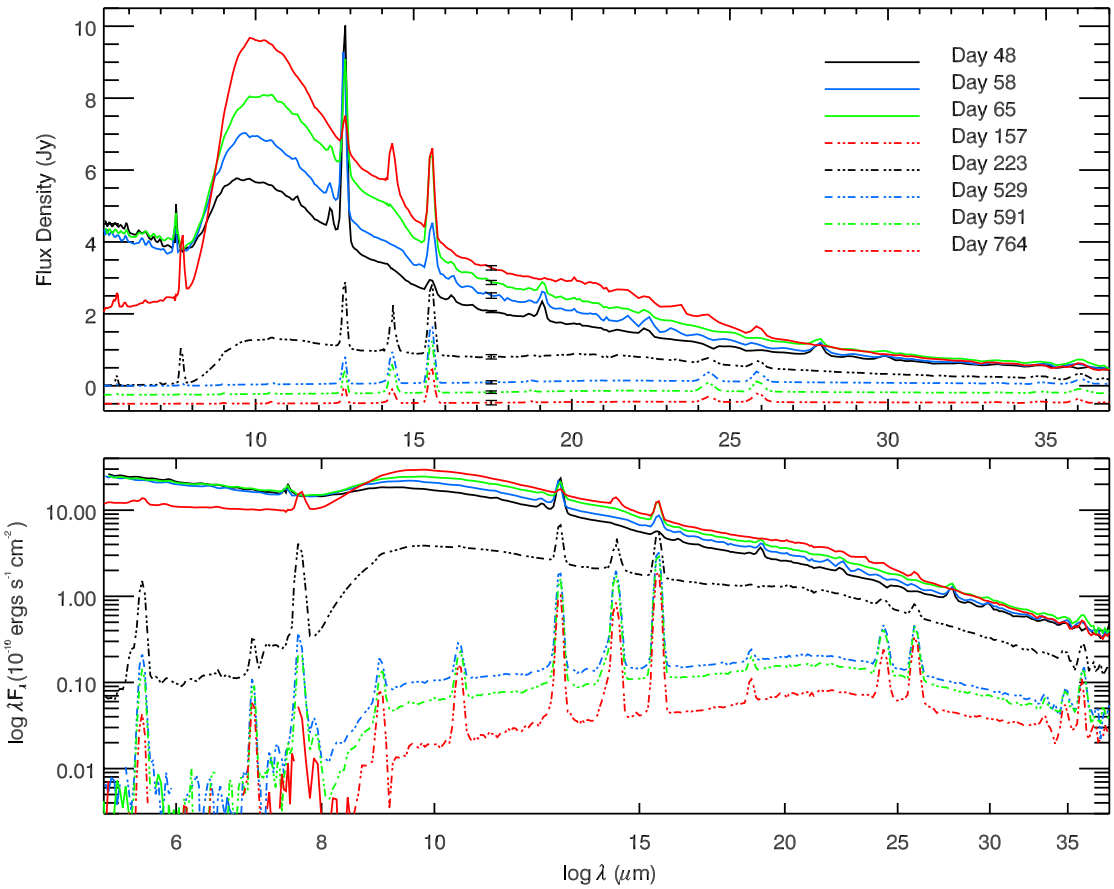

Figure 5. Evolution of the *Spitzer* low-resolution IRS spectra. Top: *Spitzer* spectra in Fν vs. linear λ highlighting the strong 10 μm silicate dust feature that appeared. The final three observations only, including the day 529 (2008 July 2), day 590 (2008 September 2), and day 763 (2009 February 22) data, have been multiplied by a factor of 10 and offset for clarity. The error bars presented at 17.5 μm show representative 3σ errors for each epoch. Bottom: same spectra in λF_λ vs. log λ. The data in this plot have not been scaled.

Table 4
Spitzer Spectroscopic Observation Log

Observation Date	JD (+2,450,000)	PID	Source/Background AOR	Time on Source (s) SL	SH	LL	LH	Age[a] (Days)
			Epoch 2					
2007 Mar 08.78	4168.28	30007	17677568/824	140	300	140	140	47.46
2007 Mar 18.99	4178.49	30007	17678080/336	140	300	140	140	57.67
2007 Mar 26.22	4185.72	30007	17679616/872	140	300	140	140	64.90
			Epoch 3					
2007 Jun 25.95	4277.45	30007	17683200/456	140	300	300	600	156.63
2007 Aug 30.84	4343.34	40060	22265088/344	140	300	140	140	222.52
2008 Jul 02.70	4650.20	50011	25192960/3216	140	300	300	600	529.38
2008 Sep 02.14	4711.64	50011	25198080/336	140	300	300	600	590.82
2009 Feb 22.04	4884.54	50011	25201408/664	140	300	1200[b]	600	763.72

Notes.
[a] From 2007 Jan 20.32 (JD 2,454,120.82).
[b] Order 1 was exposed for 1200 s, while Order 2 was exposed for only 720 s.

typically had spherical shells of emission embedded with knots of higher density material, while CNe having the polar blob/equatorial ring morphology were in the "slow" class. Slavin et al. (1995) posited that this difference in morphology was due to the duration of time that the ejecta were subject to sculpting in the common envelope phase. If such arguments are applicable to V1065 Cen, then the ejecta of this nova are likely to have a spherically symmetric morphology. For our subsequent analysis, we assume a spherically symmetric shell of ejecta. It is apparent, however, that spatially resolved imaging of V1065 Cen is needed to establish the true distribution of the ejecta.

3.2.2. Epoch 2 (E2)—Early Nebular Spectrum

Observations resumed on day 70 (2007 March 31), after a break of nearly 40 days, during which substantial changes in the ejecta took place. These observations indicated that permitted emission from iron had nearly disappeared, giving way to the first unambiguous appearance of nebular emission from oxygen

Table 5
Line Identifications and Fluxes from *Spitzer* IR Spectra[a]

Identification	λ (μm)	Modules[b]	Epoch 2			Epoch 3				
			2007 Mar 8	2007 Mar 18	2007 Mar 26	2007 Jun 25	2007 Aug 30	2008 Jul 2	2008 Sep 2	2009 Feb 22
[Mg VII]	5.50	SL	...	...	...	22.2 ± 6.2	...	...	...	...
[Mg V]	5.61	SL	...	...	...	37.8 ± 0.4	25.0 ± 6.2	3.11 ± 0.23	2.10 ± 0.20	0.58 ± 0.21
H I (15–7)	5.71	SL	15.5 ± 5.6	...	...	...	...	...	...	...
Huγ (9–6)	5.91	SL	20.3 ± 5.5	...	...	...	...	...	...	...
[Mg VIII]?	5.95	SL	...	...	...	11.2 ± 1.8	...	...	...	...
H I (13–7)	6.29	SL	13.6 ± 3.5	...	...	...	...	...	...	...
[Si VII]?	6.51	SL	26.3 ± 5.9	...	19.3 ± 6.7	5.91 ± 0.49	...	...	...	...
H I (12–7)	6.77	SL	8.47 ± 2.66	...	15.6 ± 6.1	...	...	...	...	...
H I (20–8)	6.95	SL	...	...	11.1 ± 6.6	...	...	...	...	...
[Ar II]	6.98	SL	7.34 ± 2.09	...	...	...	1.47 ± 0.41	1.07 ± 0.20	0.95 ± 0.15	0.67 ± 0.21
Pfα (6–5) + Huβ (8–6)	7.46	SL	64.3 ± 16.0	41.2 ± 17.8	42.4 ± 14.0	...	...	...	...	...
[Ne VI]	7.64	SL	...	...	...	124.4 ± 0.9	70.6 ± 1.8	5.97 ± 0.48	3.79 ± 0.28	0.87 ± 0.29
[Ar V]	7.90	SL	...	...	...	...	...	0.75 ± 0.28	0.35 ± 0.20	...
[Ar III]	8.99	SL	...	...	...	...	...	1.91 ± 0.18	1.60 ± 0.13	1.11 ± 0.15
[S IV]	10.51	SL, SH	...	...	...	...	2.21 ± 0.25	3.07 ± 0.01	3.02 ± 0.1	2.21 ± 0.07
H I (9–7)	11.31	SL	7.75 ± 1.20	5.29 ± 2.54	5.01 ± 4.57	...	...	...	...	...
Huα (7–6)	12.37	SL, SH	18.2 ± 0.31	14.7 ± 2.0	10.3 ± 2.2	...	...	...	...	...
[Ne II]	12.81	SL, SH	199.9 ± 0.80	150.9 ± 3.1	117.7 ± 0.5	30.0 ± 2.1	60.9 ± 0.3	24.3 ± 0.1	21.7 ± 0.1	14.5 ± 0.10
[Mg V]	13.54	SH	...	...	...	...	0.34 ± 0.23	...	...	...
[Ne V]	14.32	SH, LL	...	...	...	32.6 ± 0.4[c]	30.6 ± 0.4	28.5 ± 0.2	26.6 ± 0.11	14.2 ± 0.13
[Ne III]	15.56	SH, LL	12.0 ± 0.85	46.2 ± 0.6	74.7 ± 2.7	54.7 ± 0.4	57.3 ± 0.6	45.7 ± 0.4	40.1 ± 0.13	29.5 ± 0.21
H I (10–8)	16.21	SH, LL	3.73 ± 0.98	4.44 ± 1.05	3.89 ± 2.18[c]	...	...	...	...	...
H I (12–9)	16.88	SH	3.07 ± 1.28	4.26 ± 0.52	5.30 ± 3.54	...	...	...	...	...
[S III]?	18.71	SH, LL	2.48 ± 0.37	15.3 ± 0.22	1.26 ± 0.35	...	0.71 ± 0.21	0.90 ± 0.07	1.08 ± 0.07	1.15 ± 0.07
H I (8–7)	19.06	SH, LL, LH	9.20 ± 0.55	6.52 ± 0.41	5.42 ± 0.53	...	...	...	...	...
H I (11–9)	22.34	LL, LH	3.66 ± 0.26	2.94 ± 0.32	2.78 ± 0.27	...	...	...	...	...
[Ne V]	24.30	LL, LH	...	...	...	3.35 ± 0.26	3.82 ± 0.23	6.30 ± 0.09	6.02 ± 0.09	4.14 ± 0.06
[O IV]	25.91	LL, LH	...	...	...	4.38 ± 0.14	3.53 ± 0.16	6.04 ± 0.06	6.20 ± 0.06	5.72 ± 0.05
H I (9–8)	27.80	LL, LH	5.22 ± 0.17	3.53 ± 0.20	3.31 ± 0.18	...	...	...	...	...
H I (12–10)	29.84	LL, LH	1.73 ± 0.20	0.96 ± 0.21	0.71 ± 0.12	...	...	...	...	...
[Si II]	34.81	LL, LH	...	...	...	...	0.72 ± 0.54	0.34 ± 0.16	0.46 ± 0.12	0.81 ± 0.12
[Ne III]	36.01	LL, LH	...	12.8 ± 0.70[d]	2.06 ± 0.75[d]	1.54 ± 0.35	1.79 ± 0.66[d]	1.47 ± 0.27	1.32 ± 0.34	...

Notes.
[a] Flux values in units of 10^{-13} erg s^{-1} cm^{-2}.
[b] Fluxes for lines observed in more than a single module are the weighted average of the flux in each module, unless noted otherwise.
[c] Detected in SH module only.
[d] Detected in LL module only.

and neon. The strongest non-Balmer emission line was [Ne III] λ3869, which indicated that the nova had transitioned from the permitted to the nebular stage of spectral development with spectral phase N_{ne} (Williams et al. 1991, 1994). Nebular oxygen emission at λλ4959, 5007 was also strong along with doubly ionized argon at λ7136. Emission lines of He I appeared at λ4471 and λ5876.

By the second epoch, the profile of the emission complex at 6330 Å had become more asymmetric. It exhibited a flat-topped blue peak with a broad red shoulder. Though the relative intensities of the two components were still not 3:1, the change in morphology could indicate that the feature was due to [O I] emission superimposed on emission from Fe II. Alternatively, the blue peak may have been due to the appearance of [S III] λ6312 blended with the emission complex observed in E1.

Careful examination of the He I λ5876 line profile reveals a shoulder corresponding to Na I λ5890. The presence of Na I at this epoch is interesting. With an ionization potential of only 5.1 eV, one would expect that sodium would be nearly all ionized at this stage. The persistence of this feature can be explained if there were regions in the ejecta with densities high enough to shield the sodium from the underlying hard radiation. By this stage of development, dust had formed in the ejecta. Indeed, the *Spitzer* spectra reveal an exceptionally strong IR dust signature at this epoch. Dust condensation is thought to progress in relatively dense regions of the ejecta (Evans & Rawlings 2008), which can then persist for years afterward (Evans et al. 2010). Shielding by this dust could readily explain the persistence of neutral sodium in the ejecta at this epoch, emission from which may be due to recombination. This is consistent with the declining signature of O I λ7773 at this epoch, which arises primarily from recombination (Rudy et al. 1989, 1991, and references therein).

Figure 4 presents the Gemini-South GNIRS observations of V1065 Cen obtained during the second epoch. The data exhibit hydrogen recombination line emission with prominent features of O I λ1.1287 μm and λ1.3165 μm, and He I λ1.0830 μm and λ2.0587 μm. These lines of oxygen and helium were at strengths only rarely observed in CNe. Nevertheless, the characteristics of these lines were quite similar to those observed in the spectra of V1974 Cyg, the prototypical ONe novae (Woodward et al. 1995). Between the first and second GNIRS observations, a span of 12 days, the fluxes in these emission lines declined sharply relative to the continuum. In the case of He I at 2.0587 μm, the

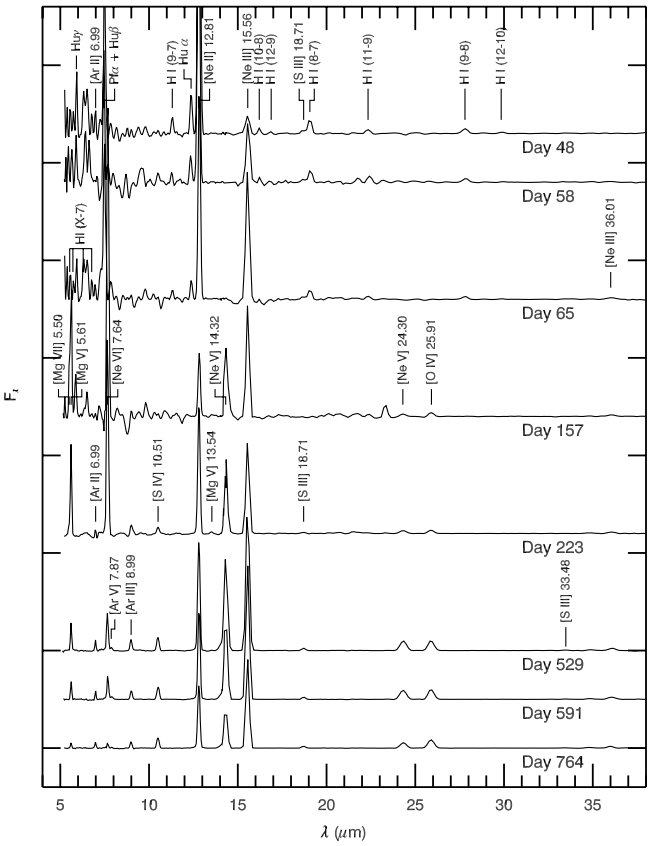

Figure 6. Evolution of the *Spitzer* low-resolution IRS spectra. The observed SEDs have been fit with a cubic spline function to remove the underlying dust continuum emission to highlight the emission lines. Continuum over-subtraction occurred in some regions of the SED, particularly near 7 μm for the day 157 (2007 June 26) data and near 8.2 μm for days 47 and 64 (08 and 2007 March 26).

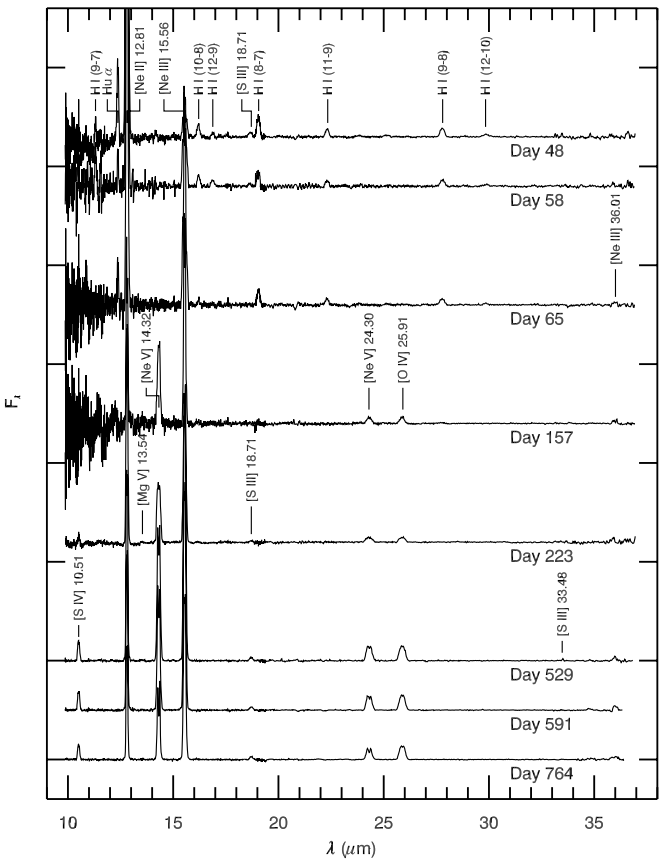

Figure 7. Evolution of the *Spitzer* high-resolution IRS spectra. The observed SEDs have been fit with a cubic spline function to remove the underlying dust continuum emission to highlight the emission lines.

flux dropped by more than an order of magnitude. This implies that conditions within the ejecta were evolving rapidly during this epoch.

The observed emission from Paη λ0.9015 μm and Paϵ λ0.9546 μm both show emission in excess of that expected for the standard recombination decrement. Based upon the emergence of [S III] in the mid-IR at this epoch (below), and the additional sulfur lines observed during E3 (Section 3.2.3), we attribute this excess to emission from [S III] λ0.9069 μm and λ0.9532 μm. A full accounting of the observed emission lines in the GNIRS data is presented in Table 3.

Figures 5–7 present a sequence of six *Spitzer* IRS low- and high-resolution spectra obtained starting in the early nebular stage of development and proceeding through nearly 800 days after outburst. To better illustrate the evolution of the emission lines, we have used the IRAF *continuum* algorithm with a *spline3* function to fit and remove the continuum emission from the data. The resultant spectra are plotted in Figures 6 and 7. The low-res continuum fits are generally very good with the exception of the regions at the ends of the short and long-wavelength spectral ranges and at the sharp increase at the blue edge of the 10 μm dust feature near 8 μm. In the day 157 SH data, there is a pronounced saw-tooth pattern arising from poor order rectification in the original BCD data. Provided the emission lines of interest are near the center of the order in these data, fitting the lines with the local continuum yields accurate line fluxes. Table 5 lists the details of the fits to the emission lines showing the evolution of the integrated line flux by epoch.

The *Spitzer* spectra acquired during the early nebular stage were dominated by a suite of hydrogen recombination lines, the strongest being the blend of Pfund α (Pfα) and Humphreys β (Huβ) at 7.46 μm. This feature, though prominent, was dwarfed by the [Ne II] λ12.81 μm emission, the strong presence of which is often used as a diagnostic for identification of an ONe nova (see Section 3.2.4). Also present in these early spectra was [Ne III] λ15.56 μm. The short wavelength spectra exhibited a surprising amount of structure with many apparent features between 5.2 and 8 μm. The central wavelengths of these features were unstable from one observation to the next making line identification difficult. An emission line at λ6.99 μm, which we tentatively identify as [Ar II], became increasingly apparent as the ejecta evolved. What may be [S III] λ18.71 μm was present, though weak, and remained throughout the evolution of the ejecta. The presence of [S III] in the IR spectra supports the hypothesis that the optical emission complex at 6330 Å was due, at least in part, to [S III] λ6312.

3.2.3. Epoch 3 (E3)—Mature Nebular Spectrum

As the ejecta of a CN continue to expand, their density declines exposing more of the ejecta to the underlying radiation field of the WD. In V1065 Cen, this was exhibited by the appearance of highly ionized species of neon, magnesium, and iron. The optical spectra were still dominated by [Ne III] and [O III], but they also revealed [Ne IV] $\lambda\lambda$4714, 4720. The IR spectra during the mature nebular stage were still dominated by emission from [Ne II] λ12.81 μm and [Ne III] λ15.56 and λ36.01 μm, but they also exhibited prominent emission from

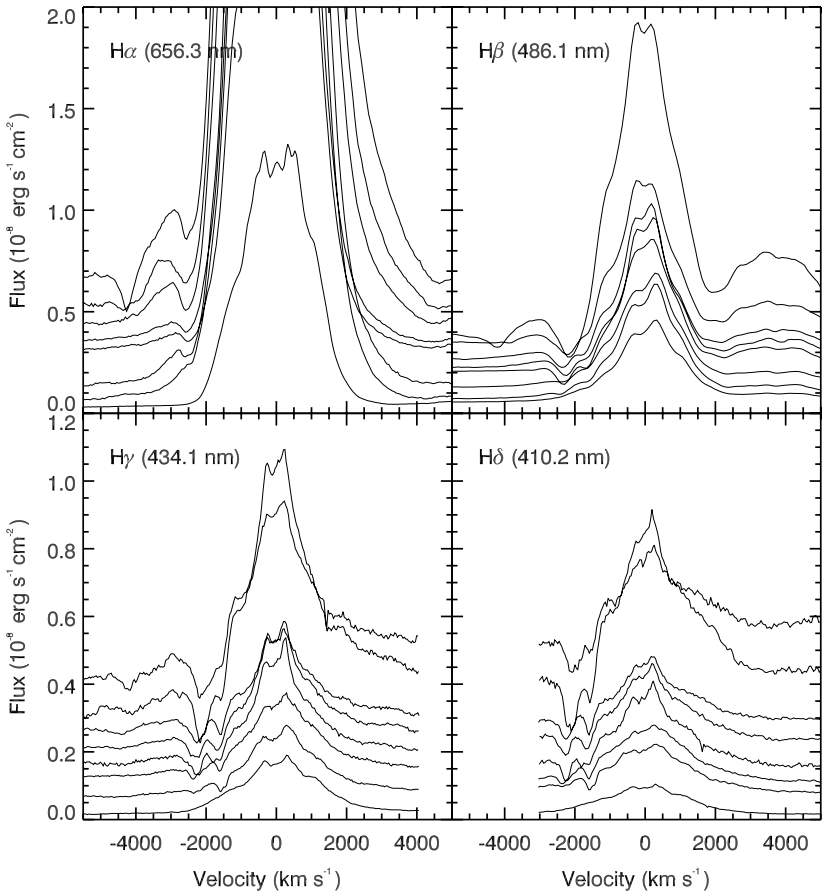

Figure 8. Evolution of the P-Cygni profiles associated with Balmer emission lines in V1065 Cen. The spectra, offest slightly in each panel for clarity, span from day 8.97 (topmost curve), Epoch 1, through day 71.80 (bottommost curve), Epoch 2. The Hα and Hβ spectra were obtained at low dispersions, while the Hγ and Hδ spectra are derived from high-dispersion observations (Section 2.2).

[Ne V] λ14.32 and λ24.30 μm along with [Ne VI] λ7.64 μm. There was also strong emission from [Mg VII] λ5.50 μm and [Mg V] λ5.61 μm and weak [Mg V] emission at λ13.54 μm.

At these late stages, many CNe also exhibit emission signatures from [Fe VI] λ5177 and [Fe VII] at λ5159, λ5276, and λ6087. In some cases, [Ca V] is observed at λ5309 and blended with [Fe VII] at λ6087 (Williams et al. 1991, 1994). These features were clearly evident during epoch 3 (E3). Due to the broad line widths, however, they were subject to blending. Interestingly, there appeared to be little, if any, emission from [Fe VII] λ5721. Based upon the transition strength alone, one would expect this transition to dominate the optical [Fe VII] emission. Hence, the features at 5305 Å and 6087 Å could be primarily due to [Ca V] with only a weak contribution from [Fe VII].

During this epoch, the emission complex at 6330 Å became narrower, more distinct, and peaked around 6310 Å. As the nebular stage progressed, the relative strength of the line near 6310 Å continued to strengthen relative to the red component of the complex, eventually growing well beyond the 3:1 intensity ratio expected for the [O I] doublet. This behavior further supports the claim that [S III] λ6312 was the dominant contributor to this feature. This conclusion was bolstered by the continued signature of [S III] λ18.71 μm and the conspicuous appearance of [S IV] λ10.51 μm in the IR.

As the H recombination spectrum faded, the presence of a shoulder on the blueward side of Hδ became apparent. Based upon the signature of various other species of sulfur in the optical and IR, the most probable identification for this line is [S II] λ4072. Interestingly, the presence of [S II] at 4072 Å without the shock induced emission features at λλ6716, 6730 leads us to conclude that shocks did not play a significant role at this late stage of evolution. This confirms that photoionization effects dominated at this epoch.

As the 6310 Å feature grew in intensity, the red component of the 6330 Å complex weakened and broadened becoming more plateau-like in appearance. It is possible that [Fe X] λ6375 was present during this late stage, but if so, it was exceedingly weak and cannot be identified with confidence. A more likely contributor to the red plateau was from [Ar V] λ6435, the companion of which was clearly present at 7006 Å. Barring reddening effects, we would expect the transition at 7006 Å to have an intensity roughly 2.4 times that at 6435 Å, consistent with what was observed.

Argon emission was observed throughout E3 in both the optical and the IR in a range of ionization states reminiscent of that observed for neon. The strongest features were [Ar II] λ6.99 μm, [Ar III] λ7136 and λ8.99 μm, and [Ar V] λ7006. But during the late stages, additional transitions of [Ar V] became visible including emission at 7.87 μm as well as the previously mentioned emission at 6435 Å.

3.2.4. Ejecta Structure

The velocity widths of the hydrogen recombination lines measured from the FWHM Gaussian line fits suggested that the lines originated in a single emitting region with an expansion velocity of 2200–2500 km s^{-1}. The widths of the lower ionization states of neon and oxygen were comparable to this and were nearly constant throughout the evolution of the ejecta. The

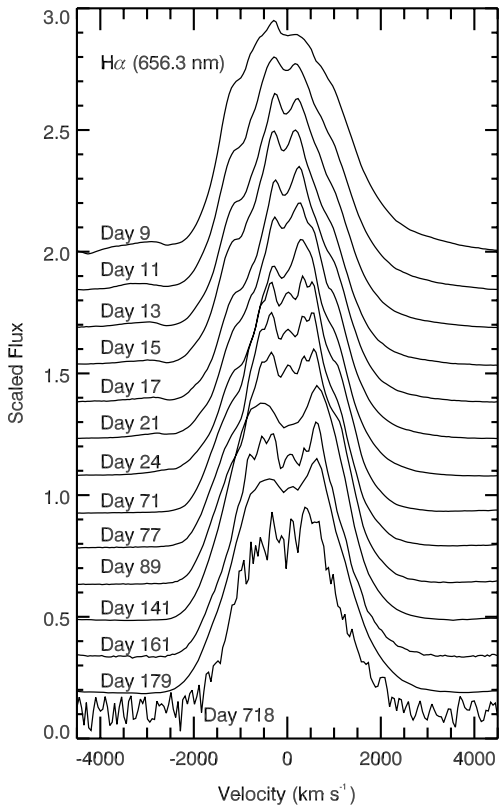

Figure 9. Evolution of the Hα line profiles throughout the evolution of the ejecta, day 9 to day 719. The profiles have been scaled to their peak value and offset for clarity.

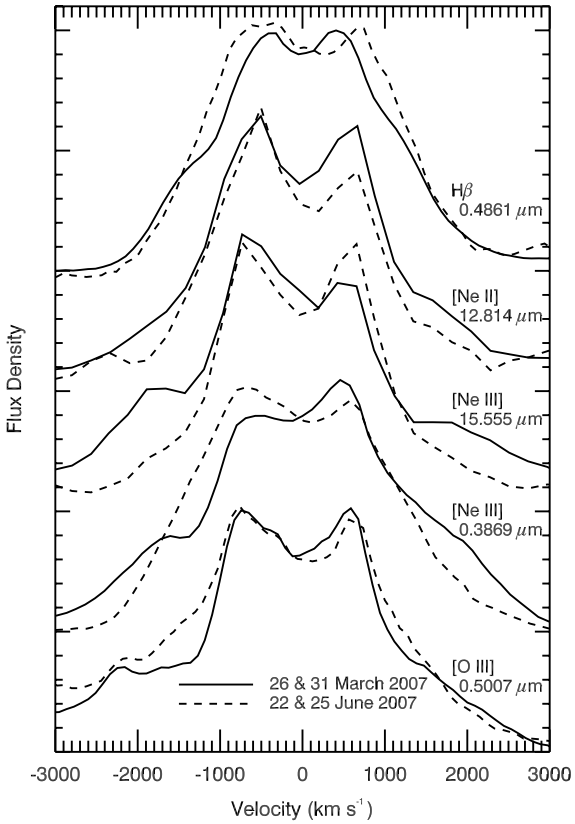

Figure 10. Line profiles of prominent emission lines in V1065 Cen. The profiles are arbitrarily normalized and offset for clarity. Line profiles from contemporaneous optical and mid-infrared observations on days 64 (2007 March 26) and 70 (2007 March 31) are depicted with solid lines, while those for days 152 (2007 June 22) and 157 (2007 June 26) are presented with dashed lines.

higher ionization states (e.g., Ne IV, Ne V, O IV) had consistently higher velocity widths at ~3500 km s^{-1} suggesting that the source of this emission was from a different and kinematically distinct region of the ejecta.

Figure 9 presents the evolution of the Hα profile with time. During E1, the profile exhibited shoulders near the peak indicating that the line was not entirely optically thin at this stage. As the ejecta expanded and the optical depth declined, the line edges became more smooth and the peak broadened. By E2, the line profile had developed somewhat flat-topped or saddle-shaped peak and the width had become fixed. Very little change was observed in the line shape after this epoch. The overall behavior of this line is consistent with a finite thickness shell that underwent nearly constant expansion.

Throughout our observations, the emission line structures were quite similar. The emission peaks had a weak saddle shape and were temporally stable. The emission line structure observed in the hydrogen recombination lines was echoed by the low-ionization emission lines such as [O III], [Ne II], and [Ne III] in both the optical and the IR. In Figure 10, we plot some of these emission lines to show the uniformity of the structure from one species and ionization state to another. The data have been scaled to the Hβ line flux and offset for clarity. The similarity of the line shapes suggested that the elemental abundance distribution was nearly uniform throughout the shell of ejecta. Models generated by Lynch et al. (2006) for an annular ejecta distribution produced saddle-shaped line profiles slightly more pronounced than that observed in V1065 Cen. This suggests that the ejecta of V1065 Cen was nearly spherical with an additional weak annular component.

Though there did not appear to be significant differences in the elemental abundances throughout the ejecta, there did appear to be density inhomogeneities. The first *Spitzer* spectra on day 47 (E2) revealed that dust was still present in the ejecta in spite of the light curve having returned to its pre-dust formation decline. As the ejecta became more optically thin, the 9.7 μm silicate feature continued to strengthen while the emission lines came to be dominated by highly ionized species such as [Ne V], [Ne VI], [Mg V], and [Mg VII]. Dust formation requires cool, dense regions in the ejecta while the formation of the highly ionized atomic species requires low density regions subjected to a hard radiation field. Further, the spectrum of V1065 Cen during E3 exhibited emission lines from atomic transitions arising from a wide range of ionization states. Ionization potentials ranged from 29.6 eV in the case of N II to 224.95 eV for Mg VII. This order of magnitude span in ionization potential supports the conclusion that by E3, there existed substantial density inhomogeneities within the ejecta. The observed low density regions were wholly subjected to energetic photons from the WD pseudophotosphere, which gave rise to emission from highly ionized atomic species, while the shielded interior of high density regions gave rise to emission from states with low ionization potential. The important role of fragmentation in the ejecta becomes apparent when modeling the observed emission (see Section 4).

3.2.5. Permitted O I Emission

The strength of O I 8446 Å ($3s^3S^0$–$3p^3P$) during the first epoch (E1) (Section 3.2.1) was remarkable. Its flux ratio relative to Hα, uncorrected for reddening, was $F_{8446}/F_{6563} = 1.0$. By the second epoch (E2), the flux ratio had declined by nearly

a factor of 20 to $F_{8446}/F_{6563} = 0.06$. Emission from O I 7773 Å ($3s^5S^0$–$3p^5P$) was significantly weaker, exhibiting a relative flux of $F_{7773}/F_{6563} = 0.06$ in E1 and 0.01 in E2. As mentioned above (Section 3.2.2), the 7773 Å transition of oxygen arises primarily from recombination and is unable to be efficiently excited by other mechanisms. For recombination alone, however, the flux of O I λ7773 should be slightly greater than λ8446 (Rudy et al. 1989). During E1 (day 22), $F_{8446}/F_{7773} = 16.7$, while at E2 (day 79), $F_{8446}/F_{7773} = 5.2$. This leads us to conclude that excitation of the 8446 Å feature was due to a mechanism other than recombination.

O I 8446 Å can also be produced through continuum fluorescence. If this were the primary excitation mechanism, then the intensity of O I 8446 Å should be significantly greater than O I 1.1287 μm. Unfortunately, the GNIRS data with coverage of the 1.1287 μm feature were obtained 18 days before the SMARTS observations of λ8446. Since the flux in the 8446 Å transition was clearly declining rapidly between E1 and E2, we cannot make a direct comparison between the two features. We can, however, compare the strength of the 1.1287 μm feature to the O I 1.3164 μm feature ($3p^3P - 4s^3S^0$), which was obtained simultaneously. Assuming excitation through continuum fluorescence alone, the 1.3164 μm flux should be slightly greater than 1.1287 μm (Rudy et al. 1989). We find that on day 47, $F_{1.1287}/F_{1.3164} = 15.2$, and on day 59, $F_{1.1287}/F_{1.3164} = 5.6$. It is unlikely, then, that continuum fluorescence played a critical role during E2.

A remaining source for excitation of O I 8446 Å is through the Bowen mechanism of Lyβ fluorescence. This process occurs due to the proximity of Lyβ λ1025.72 to O I λ1025.77 ($2p^{43}P_2$–$3d^3D^0$) (Bowen 1947). Population of the $3d^3D^0$ state results in a cascade sequence that includes transitions at 1.1287 μm ($3p^3P$–$3d^3D^0$), 8446 Å ($3s^3S^0$–$3p^3P$), and 1304 Å ($2p^3P$–$3s^3S^0$). Assuming no collisional de-excitation, the photon fluxes of 1.1287 μm and 8446 Å should be equivalent. Though our observations of these two transitions do not occur simultaneously, their exceptional line strengths support the conclusion that they arise due to Lyβ fluorescence.

For Lyβ fluorescence to be active, the optical depth of Hα must be high. Equation (1) of Rudy et al. (1989) provides an estimate for the escape probability of Hα assuming a solar abundance of oxygen. The escape probability can then be used to estimate the optical depth of Hα, $\tau_{H\alpha}$. It is clear from our analysis below (e.g., Section 4.2) that oxygen is significantly overabundant with respect to solar. Thus, the escape probability derived by this method must be scaled by the oxygen abundance relative to solar. Taking into account the high oxygen abundance, we estimate $\tau_{H\alpha} \gtrsim 150$ in E1 and $\gtrsim$50 in E2. The decline of $\tau_{H\alpha}$ is exhibited in the evolution of the P-Cyg components presented in Figure 8.

3.3. Reddening and Distance

The derivation of the distance-dependent physical parameters of V1065 Cen is heavily dependent upon the assumed reddening toward the system. An estimate of the reddening can be obtained using various techniques. One is to use the equivalent widths of optical interstellar Na I D lines detected toward the CN shortly after outburst. The Na I D absorption profiles from the first six observations of V1065 Cen have equivalent widths of 0.68 ± 0.06 Å. Using the relationship derived by Munari & Zwitter (1997) for single component Na I D1 absorption, we estimate a reddening of $E(B-V) = 1.05^{+0.55}_{-0.4}$. Assuming $R_V = A_V/E(B-V) = 3.07$, this yields a line-of-sight extinction of $A_V = 3.22^{+1.69}_{-1.23}$ mag. In many CNe, however, the Na I D absorption profiles are saturated, compromising distance determination. Since our data do not have the spectral resolution necessary to identify with certainty whether these features are saturated, we suggest that this estimate be used with extreme caution for V1065 Cen.

Alternatively, $(B-V)$ colors can be used to estimate the extinction. Research into the light curve behavior of CNe by van den Bergh & Younger (1987) revealed that the average $(B-V)$ colors for CNe at maximum light and at t_2 are 0.23 ± 0.06 mag and −0.02 ± 0.04 mag, respectively. The bottom panel of Figure 1 shows that the $(B-V)$ color of V1065 Cen near maximum light is $(B-V) = 0.52 \pm 0.04$ mag and that $(B-V) = 0.41 \pm 0.05$ mag at $t_2 = 11$ days. These values yield extinctions of $A_V^{max} = 0.93 \pm 0.22$ mag ($E(B-V) = 0.30 \pm 0.07$) at maximum light and $A_V = 1.38 \pm 0.19$ mag ($E(B-V) = 0.45 \pm 0.06$) at t_2. V1065 Cen was not observed photometrically on the rise to maximum light. Thus, A_V^{max} may be underestimated.

The Balmer decrement can be used independently to deduce the reddening. Table 6 summarizes the flux of Hα relative to Hβ for the first 160 days after outburst. Other recombination line fluxes (e.g., Hγ) were not included in the estimates of the decrement as they are blended with other lines (e.g., [O III] λ4363 Å) due to their high velocity widths. Initially, the $F_{H\alpha}/F_{H\beta}$ ratios were $\gtrsim$10, declining as the nova evolved. The measured line fluxes of Hα and Hβ at early epochs have uncertainties much larger than the formal uncertainties presented in Table 6 because of errors associated both with fitting of the associated P-Cygni absorption complexes and due to structure in the underlying continuum arising from Fe II multiplet emission. As the ejecta evolved, the continuum structure became less pronounced and the fitting uncertainties diminished. The variability in the Hα to Hβ ratio seen during the first ∼100 days was likely real, however, and not due to measurement uncertainties alone.

As late as day 58, there was strong emission from O I λ1.1289 μm (Table 3, Figure 4), while O I λ8446 persisted in the optical through day 79. As discussed above, (Section 3.2.5), these features arise due to Lyβ fluorescence. Active Lyβ fluorescence requires that Hα be optically thick. We estimate that $\tau_{H\alpha}$ was high at least until the third epoch of observations. A high optical depth in Hα violates the Case B approximation, which assumes that all non-Lyman photons are radiated away without scattering. This means that the Balmer decrement during these stages will not yield a reliable reddening estimate.

In principle, the ejecta should become increasingly transparent to Hα photons as they expand. Hence, the observed Hα to Hβ ratio should continue to decline, asymptotically approaching the intrinsic recombination ratio extinguished by reddening. Table 6 indicates, however, that at late times, there was still relatively high variability in the Hα to Hβ ratio implying that conditions within the ejecta still did not emulate the Case B approximation.

Taking this into consideration, we used the minimum observed Hα to Hβ ratio to calculate an upper limit to the reddening toward V1065 Cen. The reddening from the Balmer decrement was calculated according to

$$E(B-V) = a \times \log\left(\frac{R_0}{R}\right) \quad (2)$$

Table 6
Balmer Decrement

Obs. Date (mm/dd/yyyy)		Day	$F_{H\alpha}/F_{H\beta}$	$I_{H\alpha}/I_{H\beta}$[a]	$E(B-V)$
B band	*R* band	Number			
01/30/2007	01/29/2007	9/10	7.83 ± 0.03	2.62	1.11
02/01/2007	01/31/2007	11/12	13.24 ± 0.17	2.62	1.64
02/05/2007	02/04/2007	15/16	5.89 ± 0.02	2.62	0.82
02/07/2007	02/06/2007	17/18	6.06 ± 0.02	2.62	0.85
02/09/2007	02/10/2007	20/21	12.75 ± 0.13	2.62	1.60
02/12/2007	02/13/2007	23/24	10.73 ± 0.02	2.62	1.43
02/14/2007	02/13/2007	24/25	11.35 ± 0.11	2.62	1.48
03/31/2007	04/01/2007	70/71	6.93 ± 0.03	2.70	0.95
04/06/2007	04/07/2007	76/77	5.02 ± 0.03	2.70	0.63
04/12/2007	04/19/2007	82/89	7.01 ± 0.03	2.70	0.97
06/28/2007	06/30/2007	159/161	6.22 ± 0.03	2.85	0.79

Note. [a] Expected recombination values derived from Hummer & Storey (1987) using appropriate values for T_e and n_e.

Table 7
Reddening and Extinction

Method		$E(B-V)$	A_V[a]
Equivalent width	Munari & Zwitter (1997)	1.05 ± 0.5	3.22 ± 1.54
Color	t_{max}	0.29 ± 0.07	0.89 ± 0.21
	t_2	0.43 ± 0.06	1.32 ± 0.19
Balmer decrement		0.79 ± 0.01	2.43 ± 0.03
Extinction map	Schlegel et al. (1998)	⩽0.71	⩽2.18
Mean[b]		0.5 ± 0.1	1.5 ± 0.3

Notes.
[a] Calculated assuming $R_V = A_V/E(B-V) = 3.07$.
[b] Calculated without the equivalent width and extinction map estimates.

(Lee et al. 2003) where R is the observed flux ratio $F_{H\alpha}/F_{H\beta}$, R_0 is the intrinsic intensity ratio $I_{H\alpha}/I_{H\beta}$ for the Case B approximation (Hummer & Storey 1987), and $a = (0.4[A_1(\lambda) - A_1(H_\beta)]^{-1}$. $A_1(\lambda)$ is the extinction at wavelength λ for a reddening $E(B-V) = 1.0$, calculated using the reddening law of Cardelli et al. (1989) with a ratio of total to selective extinction $R_V = A_V/E(B-V) = 3.07$. Assuming $R_0 = 2.72$ for $T = 2\times10^4$ K and $n_e = 10^6$ cm^{-3} (Hummer & Storey 1987) yields a reddening of $E(B-V) = 0.61 \pm 0.02$. The error on the reddening estimate reflects the range of reddening values for reasonable variation in T_e and n_e. Use of alternative reddening laws such as Fitzpatrick (1999) results in differences in the derived $E(B-V)$ values of only ∼3%.

Galactic extinction maps (e.g., Schlegel et al. 1998) provide the *total* integrated extinction along the line of sight. Hence, they can provide a useful upper limit to the extinction toward V1065 Cen. Assuming that $R_V = 3.07$ in the interstellar medium (ISM), then the total extinction toward V1065 Cen normalized to the CTIO *V* bandpass is $A_V = 2.2$ corresponding to a reddening of $E(B-V) = 0.7$. Since V1065 Cen has a Galactic latitude of $b = +03.^\circ613$ and there is substantial contamination from unresolved Galactic sources in the Schlegel et al. (1998) maps near the Galactic plane ($|b| < 5^\circ$), these extinction estimates should be taken with caution.

Table 7 summarizes the various reddening and extinction estimates with their associated errors. The mean is $E(B-V) = 0.5 \pm 0.1$ ($A_V = 1.5 \pm 0.3$), which we will adopt throughout our subsequent discussion. This is comparable to the upper limit on the reddening derived from the Schlegel et al. (1998) extinction maps.

We estimate the distance to V1065 Cen using the maximum magnitude–rate of decline relationship (MMRD; della Valle & Livio 1995). For $t_2 = 11$ days, the MMRD yields an absolute magnitude of $M_V = -8.6 \pm 0.5$, where the error is estimated from the 3σ variation in the MMRD fit to the data reported by della Valle & Livio (1995). Adopting $m_{V,max} = 7.6 \pm 0.2$ and correcting with the mean extinction, $A_V = 1.5 \pm 0.3$ (Table 7), results in a distance modulus of $m_V - M_V = 14.7 \pm 0.6$. This implies a distance of $d = 8.7^{+2.8}_{-2.1}$ kpc to V1065 Cen. Recent work by Del Pozzo (2005) examining CNe in the Large Magellanic Cloud has indicated that there is a much higher uncertainty in the relationship between $m_{V,max}$ and M_V for ONe novae than for CO novae. Hence, the MMRD relation may not be valid for ONe novae and the derived distance for V1065 Cen may not be well constrained.

4. PHOTOIONIZATION MODELING

Photoioinization models provide estimates of ejecta abundance and density as well as source luminosity and temperature. Modeling of multiple epochs also enables assessment of whether abundance patterns change as the ejecta evolve and the radiation field varies. The Cloudy photoionization code, C07.02.02 (Ferland et al. 1998) was used to model the line emission observed on 2007 March 20–April 01 (Epoch 2; days 58–70) and 2007 June 26–30 (Epoch 3; days 157–160). Cloudy generates predictions of output spectra from non-LTE, illuminated gas clouds by solving the equations of thermal and statistical equilibrium for a given set of input parameters. We assumed a spherically symmetric, expanding shell morphology. The inner and outer shell radii were calculated using the minimum and maximum expansion velocities as determined from the average FWHM of the emission lines (2400 km s^{-1}) and the maximum P-Cygni absorption velocity (4250 km s^{-1}), respectively. The ejecta density was assumed to follow a power law, $\rho \propto r^{-\alpha}$ with $\alpha = 3.0$ for a shell undergoing ballistic expansion, and the covering factor was set to unity. The abundances of all elements were held fixed at their solar values except for He, N, O, Ne, Mg, Ar, S, and Fe. The difference between the number of observed emission lines (n) and the number of free parameters (n_p) gives the number of degrees of freedom (dof), $\nu = n - n_p$. The model free parameters included the source temperature, source luminosity, electron density (n_e), and the aforementioned elemental abundances, yielding a total of 11 free parameters. Tables 8–11 display the best-fit models and parameters for E3 and E2 along

Table 8
Best-fit Cloudy Models—Epoch 3

Line ID	λ (μm)	Observed[a]	One Component		Two Component	
			Modeled	χ^2	Modeled	χ^2
Optical (Days 153, 159, 161)						
[Ne III]	0.3869	12.13	11.99	0.00	12.09	0.00
[Ne III]	0.3968	3.83	3.61	0.05	3.64	0.04
H I	0.4340	0.36	0.52	3.01	0.51	2.69
[O III]	0.4363	1.82	1.96	0.11	2.09	0.36
He II	0.4686	0.20	0.12	1.03	0.17	0.15
[Ne IV]	0.4720, 0.4725	1.95	1.66	0.55	1.95	0.00
H I	0.4861	1.00	1.00	0.00	1.00	0.00
[O III]	0.4959	1.29	1.13	0.24	1.11	0.30
[O III]	0.5007	3.86	3.40	0.23	3.33	0.30
[Fe VII] + [Fe VI]	0.5159, 0.5177	0.09	0.08	0.10	0.09	0.01
[N II]	0.5755	0.52	0.39	0.67	0.49	0.04
He I	0.5876	0.26	0.29	0.36	0.26	0.00
[S III]	0.6312	0.51	0.57	0.14	0.55	0.07
H I	0.6563	4.01	3.58	0.29	3.42	0.55
He I	0.6678	0.10	0.07	0.58	0.07	1.04
[Ar V]	0.7007	0.06	0.07	0.12	0.08	0.60
He I	0.7065	0.21	0.23	0.04	0.21	0.01
[Ar III]	0.7135	0.47	0.51	0.03	0.41	0.11
[Ar III]	0.7751	0.18	0.12	0.66	0.10	1.29
Mid-IR (Day 157)						
[Mg VII]	5.5030	0.28	0.01	10.27	0.20	1.05
[Mg V]	5.6100	0.48	0.08	7.58	0.59	0.57
[Ne VI]	7.6520	1.57	0.07	10.09	1.22	0.54
[Ne II]	12.8100	0.29	0.39	1.48	0.44	3.46
[Ne V]	14.3200	0.41	0.03	9.68	0.40	0.00
[Ne III]	15.5550	0.68	0.18	6.13	0.19	5.88
[Ne V]	24.3100	0.04	0.00	9.58	0.05	0.22
[O IV]	25.9100	0.05	0.01	9.15	0.05	0.12
[Ne III]	36.0100	0.02	0.01	5.20	0.01	4.95
Total χ^2				75.96		24.35

Note. [a] All lines are normalized to Hβ.

with the dof and the calculated reduced χ^2, where $\chi^2_{\rm red} = \chi^2/\nu$ for the free model parameters n_p.

The χ^2 goodness of fit of a given model to the observed spectral energy distribution (SED) was determined from

$$\chi^2 = \sum_{i=1}^{n} \frac{(M_i - O_i)^2}{\sigma_i^2}, \quad (3)$$

where n is the number of emission lines used in the model, M_i is the modeled ratio of line flux to hydrogen line flux, O_i is the measured flux ratio, and σ_i is the error in the observed flux ratio. To minimize errors associated with flux calibration between dates and wavelength regime, we calculate the modeled and observed flux ratios relative to prominent hydrogen lines within a given wavelength regime when available, i.e., relative to Hβ in the optical, Paschen β in the near-IR, and Humphreys α in the mid-IR. Unless stated otherwise, the error estimates ranged from 10% to 30%, depending upon the strength of the line relative to continuum, the possibility of line blending with unidentified emission or atmospheric absorption features, and the formal calculated error in the measured line flux.

The measured line fluxes were dereddened using $E(B-V) = 0.5$ and compared to the output of each Cloudy model to calculate a reduced χ^2 for the fit. The model electron density was constrained by the ratio of [O III] λ4363 to [O III] λ4959 + λ5007, while limits on the source luminosity and temperature where determined from the ratio of [Ne III] λ15.56 μm to [Ne II] λ12.81 μm. The parameters from the resulting best-fit model were then applied to the near-IR observations.

4.1. Epoch 3

E3 exhibited a much greater variety of emission line species and hence provided a more robust set of constraints than E2. Consequently, we modeled this epoch first. The data used to construct the model spanned days 141–161. For simplicity, we assumed that changes occurring in the spectrum during this period were minimal. This is undoubtedly not the case. During this interval, we expect both the conditions in the ejecta and the source illumination to have undergone considerable changes. Examination of the data ranging from ∼6600 to 7000 Å in Figure 3 reveals that during this interval the line fluxes of some species were nearly constant while others varied considerably. In particular, the fluxes of [N II] λ5755 and [S III] λ6312 declined by 20%–30%. Therefore, we assume a relatively high error of 40% on optical emission line fluxes of [N II] λ5755 and of lines at wavelengths longer than 7000 Å.

The dereddened fluxes for the Balmer lines Hγ, Hδ, and Hϵ, were much greater than predicted by the Balmer decrement. For Hγ, we attribute this discrepancy to blending with the [O III] λ4363 line (Figure 3), while the Hϵ line is contaminated by

[Ne III] λ3988. The source of additional emission in the Hδ line is unclear, but may be due to [S II] λ4072 or [Fe V] λ4072. We removed the flux predicted by the dereddened Balmer decrement and attributed the remaining flux to the blended forbidden lines. Due to the high uncertainties, we did not include these hydrogen lines in our models.

Our initial attempts to model the E3 data with only a single density regime failed to achieve a suitable fit to the data. The best fit for a single-component model yielded a total χ^2 of 75.96 with a $\chi^2_{\rm red}$ of 4.75. The emission lines for the best-fit model are presented in Table 8 and the best-fit Cloudy parameters are summarized in Table 9. The derived abundances in Table 9 are given as the log abundance by number relative to hydrogen with the number of lines used in the model calculation given in parentheses. The more lines used in the model, the greater the certainty in the modeled abundance. We stress, however, that all solutions are non-unique. The total number of lines and free parameters used in calculating the reduced χ^2 from the best-fit model χ^2 are provided.

A single-component model was clearly unable to reproduce the range of ionization states observed in the ejecta. For example, emission lines from [Ne II] to [Ne IV] were fit quite well, yet the more highly ionized species of [Ne V] and [Ne VI] were underestimated by orders of magnitude. The case of magnesium is more complicated. Though these lines were underestimated by a substantial amount, a simple increase in the magnesium abundance improved the fits to the Mg emission lines while degrading the global fit. Hence, the magnesium abundance was constrained by the global model as well as by the emission lines.

As discussed above, there is strong support for the conclusion that by E3, the ejecta had differentiated into regions of higher and lower density. Following the assumption that the ejecta did not have a homogeneous density distribution during E3, we attempted to model the observed emission with a two-component model following the method of Vanlandingham et al. (2005). In this model, we assumed that the ejecta were composed of two different density regimes but that the abundances were uniform throughout. Both density components had an associated covering factor, the sum of which was unity. This effectively increased the number of parameters by two ($n_p = 13$), one additional density component and the ratio of high to low density covering factors. Hence, there were 14 dof. We conducted the modeling in a manner similar to that for a single component, but combined the predicted fluxes of the low and high density components when comparing to the observed flux ratios.

The resulting best-fit model had a total χ^2 of 24.4 with a $\chi^2_{\rm red}$ of 1.7. The two-component model greatly improved the overall fit to the more highly ionized species.

Table 9
Best-fit Cloudy Model Parameters—Epoch 3

Parameter	One Component	Two Component
log $T_{\rm BB}$ (K)	5.80 ± 0.03	5.78 ± 0.04
log luminosity (erg s^{-1})	38.27 ± 0.10	38.15 ± 0.02
log $n_{\rm H,diff}$ (cm^{-3})	7.80 ± 0.03	6.73 ± 0.01
log $n_{\rm H,clump}$ (cm^{-3})	...	7.79 ± 0.05
α[a]	−3.0	−3.0
log $R_{\rm in}$ (cm)[b]	15.44	15.44
log $R_{\rm out}$ (cm)[c]	15.76	15.76
Filling factor	0.10	0.10
Power[a]	0.0	0.0
Covering factor (diffuse)	1.00[a]	0.49 ± 0.04
Covering factor (clump)	...	0.51 ± 0.04
He[d]	−0.81 ± 0.07 (4)	−0.82 ± 0.05 (4)
N	−1.90 ± 0.10 (1)	−1.82 ± 0.06 (1)
O	−1.50 ± 0.11 (4)	−1.42 ± 0.03 (4)
Ne	−1.53 ± 0.03 (9)	−1.46 ± 0.04 (9)
Mg	−2.74 ± 0.22 (2)	−2.75 ± 0.11 (2)
S	−2.97 ± 0.08 (1)	−2.93 ± 0.18 (1)
Ar	−3.86 ± 0.10 (3)	−3.90 ± 0.13 (3)
Fe	−3.40 ± 0.16 (1)	−3.68 ± 0.13 (1)
Ejected gas mass	1.0×10^{-3}	1.7×10^{-4}
Number of lines	27	27
dof	16	14
Total χ^2	75.96	24.35
Reduced χ^2	4.75	1.74

Notes.
[a] This was not a free parameter in the model.
[b] Calculated assuming a minimum expansion velocity of 2400 km s^{-1} over 157 days and was not a free parameter in the model.
[c] Calculated assuming a maximum expansion velocity of 4250 km s^{-1} over 157 days and was not a free parameter in the model.
[d] The log abundance by number relative to hydrogen. All elements not listed in the table above were set to their solar values. The number of lines used in determining each abundance estimate is given in parentheses.

4.2. Epoch 2

We then applied the abundance solution derived for E3 to the days 58–70 data in E2. The spectral coverage of the data used in this epoch's analysis was more broad, including optical, near-IR, and mid-IR data, but exhibited fewer elemental species and a more limited range of ionization states. During this interval, the emission lines were changing rapidly. To minimize the effect of these changes between the times when each bandpass was observed, each wavelength regime, optical, near-IR, and mid-IR, was modeled independently and the subsequent χ^2 values were combined. The optical emission lines were modeled relative to Hβ, the near-IR lines to Paβ, and the mid-IR lines to Huα. After an initial solution was obtained using the derived abundances from E3, we then adjusted the abundances of elements that had associated emission lines while keeping the other abundances fixed at the E3 values. Again, this was done in a self-consistent manner within individual bandpasses. We derived an upper limit to the sulfur abundance by assuming that excess of emission in Paη and Paϵ was due to [S III].

The resulting best-fit model had a total χ^2 of 24.2 with a $\chi^2_{\rm red}$ of 1.4. The derived blackbody temperature and luminosity for the illuminating source and the shell hydrogen densities were consistent with expectations for an expanding shell morphology. The E2 modeled abundance enhancements were not found to be as extreme as in E3, but we note that this earlier epoch had fewer metal lines with which to constrain the abundances.

Though the $\chi^2_{\rm red}$ is quite good, the Cloudy model still has some significant problems. It was unable to adequately reproduce the observed emission in the complex at 6330 Å or the near-IR O I emission lines at 1.1284 μm and 1.3169 μm. There were additional problems in the near-IR modeling the He I emission at 2.0587 μm. One of the strongest lines in the near-IR spectrum, this feature was underestimated in our model by nearly 2 orders of magnitude.

Our initial models were unable to generate any significant flux from [O I] λλ6300, 6364. These transitions may, however, be excited by gas warmed by hot dust in the photo-dissociation region. To explore this possibility, we included continuum dust emission with a composition and grain size distribution predicted by our Dusty model (Section 5). The effects of depletion of the gas-phase elements into the dust grains was

Table 10
Best-fit Cloudy Models—Epoch 2

Line ID	λ (μm)	Observed	Modeled	χ^2
Optical[a] (Days 70, 71, 79)				
[Ne III]	0.3869	1.63	1.47	0.24
[Ne III]	0.3968	0.40	0.44	0.10
H I	0.4340	0.48	0.58	0.48
[O III]	0.4363	0.34	0.30	0.12
H I	0.4861	1.00	1.00	0.00
[O III]	0.4959	0.25	0.26	0.03
[O III]	0.5007	0.74	0.77	0.03
[N II]	0.5755	0.10	0.10	0.01
He I	0.5876	0.25	0.27	0.10
[S III]	0.6312	0.10	0.14	2.22
H I	0.6563	3.89	5.27	3.13
He I	0.6678	0.09	0.07	0.64
Near-IR[b] (Day 59)				
H I	0.9015	0.12	0.14	0.19
[S III]	0.9069	0.33	0.21	1.58
[S III]	0.9532	0.43	0.51	0.37
H I	0.9546	0.29	0.23	0.46
H I	1.0050	0.36	0.34	0.23
He I	1.0830	8.16	9.64	0.81
H I	1.0940	0.61	0.55	0.12
He I	1.2530	0.07	0.04	1.74
H I	1.2820	1.00	1.00	0.00
H I	1.6810	0.10	0.05	2.91
H I	2.1660	0.15	0.15	0.03
Mid-IR[c] (Day 65)				
H I	11.3100	0.56	0.32	4.52
H I	12.3700	1.00	1.00	0.00
[Ne II]	12.8100	13.04	13.01	0.00
[Ne III]	15.5550	8.69	7.52	0.81
H I	19.0600	0.60	0.42	0.93
H I	27.8000	0.36	0.20	2.32
[Ne III]	36.0100	0.23	0.29	0.84
Total χ^2				22.75

Notes.
[a] Normalized to Hβ.
[b] Normalized to Paβ.
[c] Normalized to Huα.

Table 11
Best-fit Cloudy Model Parameters—Epoch 2

Parameter	Value
log T_{BB} (K)	4.77 ± 0.02
log luminosity (erg s^{-1})	38.05 ± 0.09
log $n_{H,diff}$ (cm^{-3})	6.97 ± 0.24
log $n_{H,clump}$ (cm^{-3})	8.24 ± 0.04
α[a]	−3.0
log R_{in} (cm)[b]	15.16
log R_{out} (cm)[c]	15.40
Filling factor	0.10
Power[a]	0.0
Covering factor (diffuse)	0.57 ± 0.05
Covering factor (clump)	0.43 ± 0.05
He[d]	−0.94 ± 0.07 (4)
N	−2.36 ± 0.07 (1)
O	−1.72 ± 0.16 (3)
Ne	−1.72 ± 0.08 (5)
Mg[e]	−2.75 ± 0.11 (...)
S	−3.60 ± 0.12 (2)
Ar[e]	−3.90 ± 0.13 (...)
Fe[e]	−3.68 ± 0.13 (...)
Ejected gas mass	1.4×10^{-4}
Number of lines	27
Degrees of freedom	16
Total χ^2	22.75
Reduced χ^2	1.42

Notes.
[a] This was not a free parameter in the model.
[b] Calculated assuming a minimum expansion velocity of 2400 km s^{-1} over 70 days and was not a free parameter in the model.
[c] Calculated assuming a maximum expansion velocity of 4250 km s^{-1} over 70 days and was not a free parameter in the model.
[d] The log abundance by number relative to hydrogen. All elements not listed in the table above were set to their solar values. The number of lines used in determining each abundance estimate is given in parentheses.
[e] This was set to the abundance value derived for E3.

considered in estimating the abundances. The inclusion of dust to the photoionization model resulted in little additional [O I] flux and had only a marginal (⩽10%) affect on the calculated model abundances. The weak impact of metal depletion onto the dust grains is not surprising if the dust to gas ratio was very low in the ejecta of V1065 Cen (Section 5).

As mentioned above (Section 3.2.3), the E3 IR spectra clearly reveal the presence of sulfur in the ejecta, which suggests that the 6330 Å emission complex could also be due to [S III] λ6312 Å. The predicted model flux from sulfur is given in Table 10 and likely accounts for much of the observed emission in this complex.

During this epoch, the best-fit models predicted high optical depths in Hα and Lyβ, $\tau_{H\alpha} = 25$ and $\tau_{Ly\beta} = 7.0 \times 10^7$. The Cloudy prediction for $\tau_{H\alpha}$ is consistent with our estimate based upon the observed intensity ratio of O I λ8446 to Hα at this epoch. In spite of this, our models underestimated the flux in the O I emission lines at 8446 Å, 1.1284 μm, and 1.3169 μm significantly. In part, we attribute these difficulties to the complexity in reproducing the excitation mechanisms governing the O I emission, including Lyβ fluorescence, and to a lesser extent, recombination and continuum fluorescence (Section 3.2.5). Further, even the two-component models likely fail to adequately reproduce the complicated density structure characterizing the ejecta. The conditions in the regions in which these lines originate are likely not accurately reproduced. A detailed solution for the neutral oxygen emission, correctly encapsulating the above affects into photoionization models is beyond the scope of this paper, and thus, we excluded these line fluxes from consideration in estimating the goodness of fit for all photoionization analysis.

The Cloudy model significantly underestimated the flux in He I λ2.06 μm ($2p^1P_1^0$–$2s^1S_0$). The excitation mechanisms for this transition are complex. The transition arises from the $2p^1P_1^0$ level, which can decay either to the $2s^1S_0$ level at 2.06 μm or to the $1s^21S$ level at 584 Å. The branching ratio for these transitions is ∼10^{-3}:1, but under Case B conditions, the λ584 transition is optically thick, potentially enhancing emission at 2.06 μm through resonant scattering. The rate of fluorescence is dependent upon T_e, n_e, the He abundance and ionization fraction, and the presence of dust (Shields 1993; DePoy & Shields 1994; Luhman et al. 1998). We conclude that extreme flux of He I λ2.06 μm line is probably due to the high optical depth in the 584 Å transition. Hence, the He I λ2.06 μm emission line was excluded from consideration during the χ^2 minimization to determine the best-fit model parameters.

We calculated the average abundances by taking the linear mean of the abundances derived for E3 and E2. The average abundances by number relative to hydrogen are shown in Table 13. Overall, our best-fit models suggest a moderate overabundance of helium and iron in the ejecta, with abundances by number, relative to solar of $\mathrm{He/H} = 1.6 \pm 0.3$ and $\mathrm{Fe/H} = 6.6 \pm 2.3$. The abundances of O, Mg, S, and Ar were all significantly enhanced with $\mathrm{O/H} = 58 \pm 18$, $\mathrm{Mg/H} = 45 \pm 13$, $\mathrm{S/H} = 54 \pm 31$, and $\mathrm{Ar/H} = 50 \pm 18$. Neon and nitrogen were both found to be heavily enhanced relative to solar. The nitrogen abundance was $\mathrm{N/H} = 144 \pm 34$ and the neon abundance was even greater, $\mathrm{Ne/H} = 316 \pm 58$. All relative abundances are based upon the solar abundance values reported by Asplund et al. (2009).

Models of the TNR predict very little enhancement of iron in the ejecta. Consequently, the observed overabundance of iron suggests that hydrogen in the ejecta is significantly depleted. One explanation for the high abundances is that a substantial mass of material was dredged up from the underlying WD (Truran & Livio 1986). On the other hand, the high sulfur abundance may imply "breakout" from the CNO cycle. Recent models of TNR on slowly accreting massive WDs were able to produce conditions capable of breakout from the hot CNO cycle resulting in enhancements of the sulfur abundance (Glasner & Truran 2009). The predicted sulfur enhancement was moderate, however, and still would not account for the observed overabundance. Further, the errors on the sulfur abundance determined by the Cloudy models are quite high, so related conclusions must be taken with extreme caution. The most probable explanation for the observed overabundances is due to dredge-up from the ONe WD.

The high neon enhancement clearly indicates that V1065 Cen is an ONe nova and situates it at the upper extreme of the class. The high neon abundance invites comparison to other ONe CNe such as V838 Her, which had a neon abundance of ~180 times solar (José & Shore 2008). Besides the similarities in the neon enhancement, both of these objects were also overabundant in helium and sulfur. For V838 Her, He and S were 1.4 and 27.9 times solar, respectively.

4.3. Ejecta Mass Estimates

The mass of hydrogen in the ejecta can be estimated using the techniques described by Vanlandingham et al. (2005). Adopting their approach, the ejecta were divided into 1000 nested shells using the inner and outer radii calculated above (Tables 9 and 11). The density within each shell was computed from model best-fit density distribution where n_{H} is the density at the inner radius. Likewise, we applied the filling factor to each shell—in this case at a constant value of 0.1 throughout. We then determined the total shell mass and multiplied by the covering factor to estimate a final ejected mass. The best-fit model for E2 predicts a shell mass of $1.4 \times 10^{-4}\ M_{\odot}$. For E3, the sum of the contribution from the diffuse and clump components yields an ejected mass of $1.7 \times 10^{-4}\ M_{\odot}$. The average ejecta mass derived for V1065 Cen, $1.6 \times 10^{-4}\ M_{\odot}$, is comparable to that estimated in other ONe CNe, such as V1187 Sco ($\sim 10^{-4}\ M_{\odot}$; Lynch et al. 2006) and V1974 Cyg ($\sim 2 \times 10^{-4}\ M_{\odot}$; Vanlandingham et al. 2005).

5. DUST

In CNe, dust formation occurs if the local density and temperature in the ejecta are commensurate with the physical conditions required for grain condensation (Gehrz 2008). The resultant obscuration of the central source at the time of the condensation event is characterized by a marked inflection in the decline of the broadband optical light curves, especially at blue wavelengths, and recovery as the dust formation subsides in the expanding ejecta. The depth of the transition in the light curve enables estimation of the optical depth, τ_V, of the dust at maximum extinction. The *B*- and *V*-band light curves of V1065 Cen (Figure 2) both exhibit a shallow dip and recovery that we interpret as a dust condensation event. The optical depth of the extinction event in the *V* band is $\tau_V = 1.06 \pm 0.06$, while $\tau_B = 0.97 \pm 0.07$, $\tau_R = 0.31 \pm 0.05$, and $\tau_I = 0.27 \pm 0.09$, for the *B*, *R*, and *I* bands, respectively.

The optical extinction appears to be relatively flat in the *B* and *V* bands, i.e., at wavelengths below about 5800 Å. The break in the absorption efficiency between the *V* and *R* bands allows us to make a rough estimate of the dust grain radius. If we assume that the dust grains are of uniform size, then the extinction curve will be relatively flat or "gray" when,

$$\frac{2\pi a}{\lambda} > 1, \tag{4}$$

where a is the grain radius. Equation (4) yields an approximate grain size of $a \gtrsim 0.09\ \mu$m. This is necessarily an oversimplification since in reality the dust will have a much more complicated grain size distribution. Nevertheless, we consider this to be a reasonable first-order estimate.

The dust mass in the ejecta can be deduced from

$$M_{\mathrm{d}} = \frac{16\pi}{3} \frac{R^2 \tau_V a \rho_{\mathrm{gr}}}{Q_{\mathrm{abs}}} \tag{5}$$

(Gehrz et al. 1995), where $R = v_0 t$, the grain density $\rho_{\mathrm{gr}} = 3\ \mathrm{g\ cm^{-3}}$ with absorption coefficients $Q_{\mathrm{abs}} \sim 0.5$ at $\lambda = 0.55\ \mu$m (i.e., for grain sizes near $a = 0.3 \mu$m; Draine & Lee 1984). Assuming that the dust originated within a region of the ejecta expanding with the average velocity $v_0 \sim 3325\ \mathrm{km\ s^{-1}}$, 33 days after outburst, we find a dust mass of $M_{\mathrm{d}} \sim 1.5 \times 10^{-8}\ M_{\odot}$.

The first IR observations of V1065 Cen were obtained about 20 days after onset of dust formation, just as the light curve was resuming its normal, post-extinction event decline. The initial *Spitzer* observations revealed a broad feature near 10 μm superimposed on a strong dust continuum. The Gemini coverage extended only to 2.5 μm while the *Spitzer* coverage began at 5.2 μm leaving a gap in the IR spectral coverage. In spite of the gap in coverage, it is apparent that at this epoch the underlying continuum mimicked a blackbody that likely peaked around 3–4 μm. We identify the broad emission feature near 10 μm as the Si–O stretching mode vibration of silicates, which typically occurs at 9.7 μm. This solid-state feature has an associated 18 μm feature caused by O–Si–O bending mode oscillations (Kwok 2007). In CNe these features are believed to arise from small (radii $\lesssim 1.0\ \mu$m) silicate grains being illuminated by the outburst and are best observed under optically thin conditions. There was no evidence for unidentified infrared features as was observed in other dust producing novae such as V705 Cas (Evans et al. 2005), DZ Cru (Evans et al. 2010), V2361 Cyg, or V2362 Cyg (Lynch et al. 2008; L. A. Helton et al. 2010, in preparation).

The IR SED of V1065 Cen evolved rapidly through the first few months post-outburst (Figure 5). Between day 47 and day 157, the underlying continuum declined sharply while the peak 9.7 μm flux density nearly doubled. Over the next 66 days,

however, the 9.7 μm flux declined by a factor of ~7. By day 529, the peak emission had transitioned to longer wavelengths, between 20 and 23 μm. From this point on, the overall shape of the SED remained steady while the total emission gradually declined. Though the shape of the SED is not well characterized by a blackbody curve, the general behavior is consistent with the gradual cooling of the dust grains. The lingering presence of highly ionized elemental species of magnesium and neon at late times ($t \geqslant$ day 529) implies that the radiation field was still quite hard. Consequently, we expect there to be ongoing grain processing at this epoch. The evidence for this, however, is not readily apparent. More detailed analysis is required to properly characterize the development of the dust at late times and to understand the active grain processing mechanisms involved.

5.1. Dusty Modeling

To better understand the composition and evolution of the dust present in the ejecta of V1065 Cen, we modeled the *Spitzer* and Gemini observations from days 57 to 58 using the Dusty radiative transport code (Ivezić et al. 1999). This program propagates incident radiation through a dust cloud accounting for the composition specific absorption and emission efficiencies to calculate the temperature distribution in the cloud and the emergent SED. We assumed a spherical ejection distribution with a power-law density distribution $\eta \propto y^{-3}$, where η is the dimensionless profile function and y is the scaled radius of the shell ($y = R/R_{\rm in}$ with $R_{\rm in}$ equal to the inner shell radius). We estimated y to be 1.8 based upon the minimum and maximum expansion velocities, 2400 and 4250 km s^{-1}, respectively. The grain size distribution (power-law index, minimum, and maximum grain sizes), the dust temperature at the inner boundary, and the relative abundances of different grain types, including two types of silicates, warm silicates from Ossenkopf et al. (1992) and silicates from Draine & Lee (1984), and AC from Hanner (1988), were free parameters in our Dusty models.

We assessed the quality of the fit through visual comparison to observations. The continuum flux levels of the Gemini data were only poorly constrained. There were significant difficulties in flux calibration of these data due in part to the source brightness, but also to poor rectification and matching of the spectral orders. Also, during E2, the continuum flux due to dust emission was changing rapidly. Between days 58 and 65, the flux density at 7 μm grew by 10% while the shape of the continuum between 5.2 and 7 μm flattened noticeably. To deal with these uncertainties, we allowed a bias level offset to be applied independently to each spectral order of the Gemini data while matching the overall slope of the near-IR SED. Since the flux calibration of the *Spitzer* data was robust, they were used to fix the modeled mid-IR continuum flux. In order to adequately fit the near-IR data, it was also necessary to include a weak free–free component of the form $\lambda F_\lambda \propto \lambda^{-0.8} \exp(-hc/\lambda kT)$. Our model for the dust in V1065 Cen is presented in Figure 11 with model parameters and output presented in Table 12.

The model for the observed SED suggests that the grains in the ejecta of V1065 Cen were comprised primarily of silicates (95% by number) with a small fraction (5% by number) of AC. The 9.7 μm feature had a broad shape that we were unable to fit using any of a wide range of model parameters but with only a single silicate grain type. In order to better match both the width of the feature and the emission peak, we included a roughly 15/4 mix of silicates with optical properties described by Draine & Lee (1984) and warm silicates described by Ossenkopf et al. (1992). Models that included no carbonaceous grains failed to match the slope of the near-IR emission and underestimated the *Spitzer* 5.2–8 μm continuum. The substitution of graphitic carbon in place of AC resulted in a worse fit overall to both the near-IR data and the *Spitzer* blue continuum data. We consider that the fraction and composition of the carbon grain component is poorly constrained.

Table 12
Best-fit Dusty Model Parameters—Epoch 2

Parameter	Value
log T_{BB} (K)[a]	5.30
$T_{\rm dust}$ at $R_{\rm in}$ (K)	1050
y	1.8[b]
α	3.0
$\tau_{9.7}$	0.20
Silicate fraction	0.95
Amorphous carbon fraction	0.05
$a_{\rm min}$ (μm)	0.005
$a_{\rm max}$ (μm)	5.000
q	3.0
$F_{\rm bol}$ at $R_{\rm in}$ (W m^{-2})	5.25×10^4
$R_{\rm in}$[c] (cm)	2.41×10^{14}
$R_{\rm in}/R_\star$[d]	4.16×10^4
θ[e] ($''$)	1.80
$T_{\rm dust}$ at $R_{\rm out}$ (K)	644

Notes.
[a] This is the blackbody temperature of the illuminating source.
[b] Calculated assuming minimum and maximum expansion velocities of 2400 and 4250 km s^{-1}, respectively, over 58 days. This was not a free parameter in the model.
[c] For a luminosity of 1×10^4 $L_\odot$.
[d] $R_\star$ is the radius of the central source. This ratio is calculated assuming an external radiation temperature of $T_e = 10{,}000$ K.
[e] Angular size when $F_{\rm bol} = 1 \times 10^{-6}$ W m^2.

Our Dusty SEDs fitted the silicate emission features poorly. Unlike silicate emission observed in many sources of astronomical silicates, in V1065 Cen, the 9.7 μm and 18 μm features are exceptionally broad and not well differentiated. Our models suggest that the relative strengths and overall shape of the two silicate peaks is a complex function of the grain size distribution and the optical depth. Increasing the maximum grain size made the features less distinct from one another, improving the fit to the inter-feature region, but at the expense of the overall strength of the silicate emission. Likewise, decreasing the optical depth resulted in an increase in strength of the emission features, but with a corresponding sharpening of the profiles.

The difficulty in fitting the shape of the silicate emission features is due in part to the optical properties used by the Dusty model. The optical properties of both the Ossenkopf warm silicate and the Draine and Lee silicate models are for environments that are intended to be representative only. The former were intended to fit warm dust in an oxygen-deficient environment (Ossenkopf et al. 1992) and the latter were a compromise between matching the observed characteristics of silicates in the "Trapezium" cluster and the absorption components arising from dark clouds (Draine & Lee 1984). None of these environments are good proxies for the ejecta of a CN. This is particularly apparent in the case of V1065 Cen. As we have discussed, the nebula from which the dust condensed was very hot and, perhaps more importantly, heavily enriched in oxygen. One would expect these extreme conditions to play an influential role in the composition and observational characteristics of the grains produced in this environment.

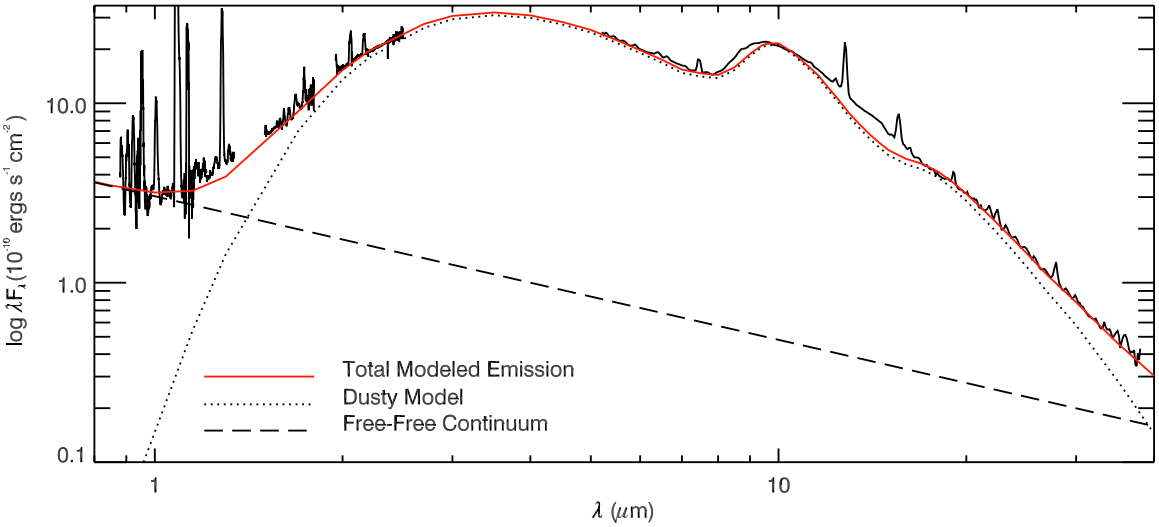

Figure 11. Plotted above are the combined Gemini and *Spitzer* data from days 58 and 57. Overlaid on the plot is the Dusty model fit with the addition of a weak underlying free–free component. See the text for discussion.

In addition, the width of the silicate emission profiles also may be influenced by the inclusion into the dust grains of high charge density cations, such as Mg^{2+} or Fe^{2+} (Nuth & Hecht 1990), both of which are present and enhanced in the ejecta of V1065 Cen (see Section 4), or emission from aluminum oxide (AlO, or Al_2O), which has been detected in the atmospheres of some evolved stars. It is also possible that the broad shape may be due to a high grain porosity. Increasing grain porosity has been shown to result in broadening of the 9.7 μm feature with a correlated blueward shift in the central wavelength of emission (Voshchinnikov & Henning 2008). Both of these characteristics are observed in the silicate features in V1065 Cen.

The presence of multiple species of dust in the ejecta of V1065 Cen, both silicates and AC, is not unusual for dust producing CNe. This chemical dichotomy can be explained if the CO nucleation sites did not saturate leaving both C and O free to form different grain types. Likewise, an inhomogeneous abundance distribution in the ejecta would allow local variations in dust production possibly coinciding with locations of higher density condensations (Evans & Rawlings 2008). We discount this latter possibility based upon the apparent uniformity in the abundance distribution throughout the ejecta.

Our models assumed dust grains with a Mathis, Rumpl, and Nordsieck (MRN; Mathis et al. 1977) power-law size distribution of the form $n(a) \propto a^{-q}$ with sharp boundaries, $a_{\rm min} \leqslant a \leqslant a_{\rm max}$. We found that a power-law index, $q = 3.0$ most accurately fitted the data. This is slightly flatter than the standard power-law index for the ISM of $q = 3.5$ and steeper than that found for the dusty nova V705 Cas ($q = 2.3$; Evans et al. 2005). The MRN size distribution for the ISM has $a_{\rm min} = 0.005\,\mu$m and $a_{\rm max} \geqslant 0.250\,\mu$m. The lower and upper limits to the grain size distribution for V1065 Cen were found to be $a_{\rm min} = 0.005\,\mu$m and $a_{\rm max} \geqslant 5.000\,\mu$m with an emission weighted mean grain size $a_{\rm avg} = 0.06\,\mu$m. The modeled minimum grain size is within a factor of 2 of the grain size estimated for a uniform size population from the dust extinction event above. Though the mass is dominated by grains that are large compared to the ISM, the lower limit to the grain size is comparable to the ISM and is not atypical of the dust grains found in CNe (cf. V705 Cas; Evans et al. 2005). The maximum grain size, however, is much larger even than that determined for other Dusty novae. As mentioned above, the 9.7 and 18 μm silicate features in V1065 Can are much less distinct than is typical, and it is this characteristic along with the underlying blackbody-like continuum that dictates the maximum grain size in the model. Due to the difficulty in fitting this region, we consider $a_{\rm max}$ to be poorly constrained.

The *V*-band optical depth determined by our Dusty modeling is $\tau_V \sim 0.5$. Though this is less than the peak optical depth of the extinction event, it is slightly higher than the observed optical depth at the time of the IR observations. This discrepancy can easily be resolved if the dust in the ejecta formed with a non-uniform, clumpy distribution. Taking this into account, the modeled extinction is consistent with the observed light curve properties.

The Dusty model predicts an inner radius of $R_{\rm in} = 2.41 \times 10^{14}$ cm for a luminosity of $L = 1 \times 10^4\ L_\odot$. This inner radius scales as $R_{\rm in} \propto L^{1/2}$. Based upon the assumption that the nova is still radiating at or near the Eddington luminosity for a 1.3 $M_\odot$ WD, this yields a predicted inner shell radius of 5.4×10^{14} cm. This is consistent with the radius calculated assuming a velocity of 2400 km s^{-1} over 58 days, $R = 6.0 \times 10^{14}$ cm.

The mass in the dust was computed assuming an r^{-3} power-law density distribution according to

$$M_{\rm d} = 8\pi R_{\rm in}^2 (1 - Y^{-2})^{-1} \ln {\rm Y} \frac{\tau_{9.7}}{\kappa_{9.7}} \qquad (6)$$

(Sarkar & Sahai 2006) where $R_{\rm in}$ is the inner radius of the dust shell, Y is the relative shell thickness, $R_{\rm out}/R_{\rm in}$, and $\tau_{9.7}$ is the model optical depth at 9.7 μm, which we find to be ~0.01. $\kappa_{9.7}$ is the dust mass absorption coefficient at 9.7 μm. We choose $\kappa_{9.7} = 1.87 \times 10^3$ by linearly interpolating across the values tabulated by Ossenkopf[25] for uncoagulated astronomical silicates. These values yield a dust mass of $M_{\rm d} = 3.7 \times 10^{-7}\ M_\odot$.

The assumptions in the Dusty model of spherical symmetry and homogeneity in the ejecta clearly contradict the conclusions drawn from the line profiles and photoionizational modeling, which indicate that the ejecta are spherically asymmetric and clumpy. Thus, the dust mass predicted by the model is likely an upper limit to the true mass of dust produced in the ejecta

[25] http://hera.ph1.uni-koeln.de/~ossk/Jena/tables.html

of V1065 Cen. On the other hand, the dust mass estimated from the optical depth of the extinction event is probably a lower limit. The majority of the optical extinction by dust condensation is due to absorption of continuum photons within the line of sight. Clumpiness in the ejecta may result in the underestimation of the dust mass contributing to the extinction event (cf. V842 Cen; Gehrz 1990). A dust mass between these extremes, $1.5 \times 10^{-8} M_{\odot} \leqslant M_{\rm d} \leqslant 3.7 \times 10^{-7} M_{\odot}$, is still high for a standard ONe nova. QU Vul, for example, only formed around $1 \times 10^{-8} M_{\odot}$ of dust (Gehrz 2008), while V1187 Sco and V1974 Cyg produced very little dust at all (Lynch et al. 2006; Vanlandingham et al. 2005, respectively).

6. CONCLUSIONS

We have assessed the properties of V1065 Centauri through examination of the light curve, Cloudy photoionizational modeling of the observed emission lines, and Dusty modeling of the solid-state emission features. We find the following:

1. The reddening toward the system is $E(B-V) = 0.5 \pm 0.1$ based upon the $B-V$ color at maximum and at t_2 and the Balmer decrement.
2. The distance calculated by the MMRD relation using the mean extinction $A_V = 1.5 \pm 0.3$ was $d = 8.7^{+2.8}_{-2.1}$ kpc.
3. The spectra reveal that this was an "Fe II broad"-type nova with a spectral evolutionary sequence of $P^{o}_{\rm fe} N_{\rm ne} A_o$ according to the CTIO classification system.
4. Our *Swift* observations did not detect a SSS phase in V1065 Cen. This implies that if this target underwent a period of SSS emission, it turned off in less than two years.
5. The abundances of He, N, O, Ne, Mg, S, Ar, and Fe by number, relative to solar were found to be He/H $= 1.6 \pm 0.3$, N/H $= 144 \pm 34$, O/H $= 58 \pm 18$, Ne/H $= 316 \pm 58$, Mg/H $= 45 \pm 13$, S/H $= 54 \pm 31$, Ar/H $= 50 \pm 18$, and Fe/H $= 6.6 \pm 2.3$. These abundance enhancements are consistent with V1065 Cen being a nova eruption arising on the surface of an ONe WD.
6. Our Cloudy models predict an ejected gas mass of $M_{\rm g} = (1.6 \pm 0.2) \times 10^{-4}\, M_{\odot}$, comparable to the ejected masses observed in other ONe novae.
7. Dusty models suggest that the dust is composed primarily of silicates (∼95%) with a possible weak contribution from AC (∼5%).
8. The dust grains were found to have a modified MRN power-law grain size distribution. The power-law slope of the distribution was $q = 3.0$ with a minimum grain size, $a_{\rm min} \sim 0.005\ \mu$m, and a maximum grain size, $a_{\rm max} \gtrsim 5.0\ \mu$m. This value of $a_{\rm max}$ is only poorly constrained.
9. Dust mass calculations from estimates of the optical depth of the dust, τ_V, yield $M_{\rm d} \sim 1.5 \times 10^{-8}\, M_{\odot}$, while calculations based upon Dusty models suggest $M_{\rm d} \sim 3.7 \times 10^{-7}\, M_{\odot}$. We take these values to represent the lower and upper limits to the true dust mass.
10. Based upon the light curve decline, the observed emission lines, the calculated abundances, and the presence of silicate dust, we classify V1065 Cen as an ONe-type CN.

A summary of the properties of V1065 Cen is provided in Table 13.

Table 13
V1065 Centauri Properties

Property	Value
Discovery	2007 Jan 23.35 = JD 2454123.85
t_0	2007 Jan 20.32 = JD 2454120.82
Equatorial coordinates	11:43:10.33 −58:04:04.3
Galactic longitude and latitude	$l = 293.9841$, $b = +03.6130$
Peak magnitude	$m_V = 7.6 \pm 0.2$ on 2007 Jan 21.04
t_2	$t_{2,V} \sim 11$ days
t_3	$t_{3,V} \sim 26$ days
Speed class	Fast
Reddening and extinction	$E(B-V) = 0.5 \pm 0.1$; $A_V = 1.5 \pm 0.3$
Distance	$d = 8.7^{+2.8}_{-2.1}$ kpc
WD type	ONe
Ejection velocity	$v_{\rm min} = 2400$ km s^{-1}
	$v_{\rm max} = 4250$ km s^{-1}
He	-0.89 ± 0.11 (1.6 ± 0.3)[a]
N	-2.00 ± 0.11 (144 ± 34)
O	-1.54 ± 0.17 (58 ± 18)
Ne	-1.57 ± 0.09 (316 ± 58)
Mg	-2.75 ± 0.11 (45 ± 13)
S	-3.14 ± 0.37 (54 ± 31)
Ar	-3.90 ± 0.13 (50 ± 18)
Fe	-3.68 ± 0.13 (6.6 ± 2.3)
Gas mass	$M_g = (1.6 \pm 0.2) \times 10^{-4} M_{\odot}$
Dust mass	$M_d = (0.2\text{–}3.7) \times 10^{-7} M_{\odot}$
Spectral sequence	$P^{o}_{fe} N_{ne} A_o$
Dust	Silicates (+ Amorphous Carbon)

Notes.
[a] The first number is the mean log abundance by number relative to hydrogen. The number in parentheses is the abundance relative to hydrogen by number, relative to solar based upon the solar values reported by Asplund et al. (2009) of He, −1.07; N, −4.17; O, −3.31; Ne, −4.07; Mg, −4.40; S, −4.88; Ar, −5.60; and Fe, −4.50.

This work is based in part on observations made with the *Spitzer Space Telescope*, which is operated by the Jet Propulsion Laboratory, California Institute of Technology, under NASA contract 1407. This work is also based on observations obtained at the Gemini Observatory, which is operated by the Association of Universities for Research in Astronomy, Inc., under a cooperative agreement with the NSF on behalf of the Gemini partnership: the National Science Foundation (United States), the Science and Technology Facilities Council (United Kingdom), the National Research Council (Canada), CONICYT (Chile), the Australian Research Council (Australia), Ministèrio da Ciència e Tecnologia (Brazil) and Ministerio de Ciencia, Tecnologìa e Innovaciòn Productiva (Argentina). Stony Brook University's initial participation in the SMARTS consortium was made possible by generous contributions from the Dean of Arts and Sciences, the Provost, and the Vice President for Research of Stony Brook University. L. A. Helton, C. E. Woodward, and R. D. Gehrz were supported in part by NASA/JPL *Spitzer* grants 1289430, 1314757, 1267992, 1256406, and 1215746 to the University of Minnesota as well as various National Science Foundation grants. D. K. Lynch and R. J. Rudy received partial support from the Independent Research and Development program of the Aerospace Corporation. S. Starrfield acknowledges partial support from NSF and NASA grants to ASU. J. Truran acknowledges support at the Argonne National Laboratory by the US Department of Energy, Office of Nuclear Physics, under contract DE-AC02-06CH11357, and by the NSF under grant PHY 02-16783 for the Frontier Center "Joint Institute for Nuclear Astrophysics." This work was also supported by the UK STFC, and various NASA Swift Grants to the investigators. We acknowledge with thanks the variable star observations from the AAVSO International Database contributed by observers worldwide and used in this research.

We also thank our anonymous referee for multiple suggestions and comments that resulted in notable improvements to the manuscript.

Facilities: Spitzer (IRS), Gemini:South (GNIRS), CTIO:1.5m

REFERENCES

Asplund, M., Grevesse, N., Sauval, A. J., & Scott, P. 2009, ARA&A, 47, 481
Bevington, P. R., & Robinson, D. K. 1992, Data Reduction and Error Analysis for the Physical Sciences (New York: McGraw-Hill)
Bode, M. F., & Evans, A. 2008, Classical Novae (2nd ed.; Cambridge: Cambridge Univ. Press)
Bowen, I. S. 1947, PASP, 59, 196
Cardelli, J. A., Clayton, G. C., & Mathis, J. S. 1989, ApJ, 345, 245
Del Pozzo, W. 2005, PhD thesis, Università di Pisa
della Valle, M., & Livio, M. 1995, ApJ, 452, 704
DePoy, D. L., & Shields, J. C. 1994, ApJ, 422, 187
Draine, B. T., & Lee, H. M. 1984, ApJ, 285, 89
Duerbeck, H. W. 2008, in Classical Novae, ed. M. F. Bode & A. Evans (2nd ed.; Cambridge: Cambridge Univ. Press)
Elias, J. H., Joyce, R. R., Liang, M., Muller, G. P., Hileman, E. A., & George, J. R. 2006, Proc. SPIE, 6269, 138
Ennis, E., et al. 1977, ApJ, 214, 478
Evans, A., & Rawlings 2008, in Classical Novae, ed. M. F. Bode & A. Evans (2nd ed.; Cambridge: Cambridge Univ. Press)
Evans, A., Tyne, V. H., Smith, O., Geballe, T. R., Rawlings, J. M. C., & Eyres, S. P. S. 2005, MNRAS, 360, 1483
Evans, A., et al. 2003, AJ, 126, 1981
Evans, A., et al. 2010, MNRAS, 406, L85
Ferland, G. J., Korista, K. T., Verner, D. A., Ferguson, J. W., Kingdon, J. B., & Verner, E. M. 1998, PASP, 110, 761
Fitzpatrick, E. L. 1999, PASP, 111, 63
Gehrz, R. D. 1990, in IAU Colloq. 122, Physics of Classical Novae 369, ed. A. Cassatella & R. Viotti (Berlin: Springer), 138
Gehrz, R. D. 1998, in ASP Conf. Ser. 137, Wild Stars in the Old West, ed. S. P. Howell, E. Kulkers, & C. E. Woodward (San Francisco, CA: ASP), 146
Gehrz, R. D. 2008, in Classical Novae, ed. M. F. Bode & A. Evans (2nd ed.; Cambridge: Cambridge Univ. Press)
Gehrz, R. D., Truran, J. W., Williams, R. E., & Starrfield, S. G. 1998, PASP, 110, 3
Gehrz, R. D., et al. 1995, ApJ, 448, 119
Gehrz, R. D., et al. 2007, Rev. Sci. Instrum., 78, 011302
Glasner, S. A., & Truran, J. W. 2009, ApJ, 692, L58
Greenhouse, M. A., et al. 1990, ApJ, 352, 307
Hack, M., Selvelli, P., & Duerbeck, H. W. 1993, NASA Special Publication 507 (Washington, DC: NASA), 261
Hanner, M. 1988, Infrared Observations of Comets Halley and Wilson and Properties of the Grains (Washington, DC: NASA), 22
Houck, J., et al. 2004, ApJS, 154, 10
Hummer, D. G., & Storey, P. J. 1987, MNRAS, 224, 801
Ivezić, Ž, Nenkova, M., & Elitzer, M. 1999, arXiv:astro-ph/9910475
José, J., & Shore, S. N. 2008, in Classical Novae, ed. M. F. Bode & A. Evans (2nd ed.; Cambridge: Cambridge Univ. Press)
Kahabka, P., & van den Heuvel, E. P. J. 1997, ARA&A, 35, 69
Kwok, S. 2007, Physics and Chemistry of the Interstellar Medium (Sausalito, CA: Univ. Science Books), 330
Lee, H., McCall, M. L., Kingsburgh, R. L., Ross, R., & Stevenson, C. C. 2003, AJ, 125, 146
Liller, W., Addiego, G., & Fonseca, W. 2007, IAU Circ., 8801, 1
Liller, W., et al. 2007, IAU Circ., 8800, 1
Luhman, K. L., Engelbracht, C. W., & Luhman, M. L. 1998, ApJ, 499, 799
Lynch, D. K., et al. 2006, ApJ, 638, 987
Lynch, D. K., et al. 2008, AJ, 136, 1815
Mathis, J. S., Rumpl, W., & Nordsieck, K. H. 1977, ApJ, 217, 425
Małek, K., et al. 2010, Adv. Astron., 2010, 9
McLaughlin, D. B. 1960, in Stellar Atmospheres, ed. B. L. Greenstein (Chicago, IL: Univ. Chicago Press), 608
Munari, U., & Zwitter, T. 1997, A&A, 318, 269
Ness, J.-U., Schwarz, G. J., Retter, A., Starrfield, S., Schmitt, J. H. M. M., Gehrels, N., Burrows, D., & Osborne, J. P. 2007, ApJ, 663, 505
Ness, J.-U., Schwarz, G. J., Starrfield, S., Osborne, J. P., Page, K. L., Beardmore, A. P., Wagner, R. M., & Woodward, C. E. 2008, AJ, 135, 1328
Ness, J.-U., et al. 2007, ApJ, 665, 1334
Nuth, J. A., III., & Hecht, J. H. 1990, Ap&SS, 163, 79
Ossenkopf, V., Henning, Th., & Mathis, J. S. 1992, A&A, 261, 567
Payne-Gaposchkin, C. 1957, The Galactic Nova (Amsterdam: North-Holland)
Rudy, R. J., Erwin, P., Rossano, G. S., & Puetter, R. C. 1991, ApJ, 383, 344
Rudy, R. J., Rossano, G. S., & Puetter, R. C. 1989, ApJ, 346, 799
Rudy, R. J., et al. 2003, ApJ, 596, 1229
Sarkar, G., & Sahai, R. 2006, ApJ, 644, 1171
Schlegel, D. J., Finkbeiner, D. P., & Davis, M. 1998, ApJ, 500, 525
Schwarz, G. J., et al. 2007, ApJ, 657, 453
Shields, J. C. 1993, ApJ, 419, 181
Shore, S. N., Sonneborn, G., Starrfield, S., Gonzalez-Riestra, R., & Ake, T. B. 1993, AJ, 106, 2408
Shore, S. N., et al. 2003, AJ, 125, 1507
Slavin, A. J., O'Brien, T. J., & Dunlop, J. S. 1995, MNRAS, 276, 353
Townsley, D. M., & Bildsten, L. 2004, ApJ, 600, 390
Truran, J. W., & Livio, M. 1986, ApJ, 308, 721
van den Bergh, S., & Younger, P. F. 1987, A&AS, 70, 125
Vanlandingham, K. M., Schwarz, G. J., Shore, S. N., Starrfield, S., & Wagner, R. M. 2005, ApJ, 624, 914
Voshchinnikov, N. V., & Henning, T. 2008, A&A, 483, L9
Werner, M. W., et al. 2004, ApJS, 154, 1
Williams, R. E. 1992, AJ, 104, 725
Williams, R. E. 1994, ApJ, 426, 279
Williams, R. E., Phillips, M. M., & Hamuy, M. 1994, ApJS, 90, 297
Williams, R. E., et al. 1991, ApJ, 376, 721
Woodward, C. E., Gehrz, R. D., Jones, T. J., Lawrence, G. F., & Skrutskie, M. F. 1997, ApJ, 477, 817
Woodward, C. E., Gehrz, R. D., Jones, T. J., & Lawrence, G. F. 1992, ApJ, 384, L41
Woodward, C. E., et al. 1995, ApJ, 438, 921